DIPLOMARBEIT

Hierarchically porous ceramics with surface functionalities structured by vat photopolymerization

ausgeführt am Institut für

Chemische Technologien und Analytik

der Technischen Universität Wien

unter der Anleitung von

Associate Prof. Dipl.-Ing. Dr.techn. Thomas KONEGGER

durch

Tobias FELSBERGER, B.Sc.

Wien 14.11.2024

Datum

Unterschrift

Abstract

Polymer-derived ceramics produced by vat photopolymerization represent a novel approach for fabricating complex monolithic structures with hierarchical porosity. In this work, preceramic polysiloxanes are combined with a secondary, sacrificial polymer compound and shaped via vat photopolymerization, during which photopolymerization-induced phase separation occurs. Through subsequent pyrolysis, ceramic SiOC materials can be obtained. As a potential use case for the hierarchically porous materials developed in this work, water purification via the removal of organic or inorganic contaminations was envisioned.

By choice of polysiloxane compounds of different carbon content, pyrolysis temperature, and complexity of the monolith geometry, functionalities such as hydrophilicity, pore size, permeability, and carbon content can be manipulated. Here, the functional group present on the polysiloxane backbone polysiloxanes was varied between a phenyl-/methyl group, to manipulate the amount of carbon introduced into the system. The pyrolysis temperature was varied between 600-800 °C, whereby the polymer-to-ceramic conversion is only fully completed at the upper end of the temperature range. In terms of part geometry, both cylinders and more complex scaffold structures could be fabricated. Methylene blue was chosen as an adsorbent to observe the potential for water purification. The concentration of the dye was measured via UV-VIS spectroscopy.

With increasing pyrolysis temperatures, the hydrophilicity of the surfaces, as well as overall permeability, were found to increase, while carbon content decreased. Pore size distribution was found to remain constant. By variation of different ratios of the polysiloxane derivates, carbon content in the final material could be controlled between 27 and 47 %, and the modal pore size ranged from 0.05 to 0.5 µm. At a pyrolysis temperature of 800 °C, increasing complexity, and increasing carbon content, adsorption capacity values of up to 3.85 $mg \cdot g^{-1}$ could be achieved.

The system established in this work shows possibilities for future application in specific wastewater removal scenarios. However, at present, the adsorption values, not coupled with other removal techniques, do not show adequate results for standalone usage.

Kurzfassung

Polymer-abgeleitete Keramiken, welche über badbasierte Photopolymerisation hergestellt werden, stellen einen neuartigen Weg dar, monolithische Strukturen mit hierarischer Porosität herzustellen. In dieser Arbeit werden präkeramische Polysiloxane mit einer polymeren Opferkomponente kombiniert. Diese werden mit Hilfe von badbasierter Photopolymerisation geformt, währenddessen eine photopolymerisations-induzierte Phasentrennung stattfindet. Durch nachfolgendes Pyrolysieren kann keramisches SiOC gewonnen werden. Die so hergestellten hierarchisch poröse Materialien können funktionalisiert werden um Abwasser von organischen Farbstoffen oder Schwermetallen zu trennen.

Durch die Auswahl von verschiedenen Polysiloxanverbindungen mit unterschiedlichem Kohlenstoffanteil, der Pyrolysetemperatur und der Komplexität der Struktur des Monolithen, können Eigenschaften wie Hydrophilizität, Porengröße, Permeabilität und Kohlenstoffanteil manipuliert werden. In dieser Arbeit werden die funktionellen Gruppen der Polysiloxane zwischen einer Phenyl- und einer Methylgruppe variiert, um den Kohlenstoffgehalt der Keramik zu beeinflussen. Die Pyrolysetemperatur wurde zwischen 600-800 °C variiert, wobei die Umwandlung zur vollständigen Keramik erst am oberen Ende des Temperaturbereichs abgeschlossen ist. Bezüglich der Probengeometrie können sowohl simple Zylinder als auch komplexere Gerüststrukturen produziert werden. Als Adsorptionsmittel wurde Methylenblau ausgewählt um das Potential für Wasseraufreinigung zu evaluieren. Die Konzentration des Farbstoffs wurde mittels UV-VIS Spektrometrie gemessen.

Es wurde festgestellt, dass bei steigender Pyrolysetemperatur die Hydrophilizität der Oberflächen sowie die Permeabilität ansteigen, während der Kohlenstoffgehalt leicht abnimmt. Die Porengrößenverteilung blieb konstant. Durch die Variation der Polysiloxanderivate in bestimmten Verhältnissen konnte der Kohlenstoffanteil zwischen 27 und 47 % und die modale Porengröße zwischen 0,05 und 0,5 µm variiert werden. Bei einer Pyrolysetemperatur von 800 °C, erhöhter geometrischer Komplexität und erhöhtem Kohlenstoffgehalt konnten Adsorptionswerte von bis zu 3,85 $mg \cdot g^{-1}$ erreicht werden.

Das in dieser Arbeit etablierte System zeigt die Möglichkeit für spezifische Abwasseranwendungen. Diese Technik ist nach derzeitigen Stand jedoch nicht geeignet, um als alleinstehende Methode für Abwasseraufbereitungen eingesetzt zu werden.

List of Abbreviations

AF	Acid fuchsin
AM	Additive manufacturing
BAPO	Phenyl-bis-(2,4,6-trimethylbenzoyl)-phosphinoxide
CIP	Ciprofloxacin
CV	Crystal Violet
DLP	Digital light processing
DMD	Digital micromirror device
DTA	Differential thermal analysis
FEG-SEM	Field emission gun – scanning electron microscopy
IUPAC	International union of pure and applied chemistry
MB	Methylene blue
Mono	Anycubic Mono 4K
PCP	Preceramic polymer
PDC	Polymer derived ceramic
Photon	Anycubic Photon D2
PSO	Polysiloxane
RB	Rhodamine B
SiOC	Silicon oxycarbide
STA	Simultaneous thermal analysis
TEOS	Tetraethyl orthosilicate
TGA	Thermal
TMPTMA	Trimethylolpropane trimethacrylate
TPM	Tripropyleneglycol methylether

Contents

1 Introduction

Topics like the global energy crisis and global warming set forth a demand for new materials and processes to guide a path to zero-emission and higher efficiency in almost all fields of science. Ceramic materials are potentially interesting participants in solving emerging challenges through their attributes. [1-3]

Ceramic materials are known for their excellent mechanical properties, which include high hardness, Young's modulus, high-temperature stability, corrosion resistance, and wear resistance. These ceramics typically come in dense form, where defects like porosity are crucial to avoid. In recent years, porous ceramics have been getting more attention due to their unique and valuable properties in various fields. [4-6]

By introducing preceramic polymers, access to the world of plastic-forming techniques (e.g., foaming, extrusion, or ejection molding) opens up to ceramic materials. One of the most flexible and fastest-growing forming techniques is light-based additive manufacturing. The layer-by-layer bottom-up approach has unique advantages. Parts with high geometrical complexity can be produced, which are hard or even impossible to produce with other forming techniques. [5, 7, 8]

In this work, vat photopolymerization is used to create hierarchically porous polymer-derived ceramics with the help of a photopolymerization-induced phase separation. This technique allows the creation of macroporous monoliths with continuous open pore networks. These materials can be used for applications like catalysis framework or water purification. [9-12]

This thesis aims to address the possibilities of steering properties of the finished ceramic and use the so-acquired knowledge for water purification. This is done by a variation of different compositions of preceramic polymer derivatives and by controlled pyrolysis, which is interrupted at various stages during the polymer-to-ceramic conversion. The best-suited parameters are then used to produce samples tailored to adsorb the dye methylene blue out of water.

This work contributes valuable insights into the development of tailoring PDCs to fit into different kinds of applications and provides a toolkit to overcome challenges appearing with those applications.

2 Objectives

The focus of this thesis was to deepen the understanding of surface attributes of polymer-derived ceramics (PDCs), the ability to direct and steer their features, and to explore their application possibilities for water purification.

The specific goals are listed and categorized as follows:

Comparison between digital light processing (DLP) and liquid crystal display (LCD) 3D-Printer

---

- Evaluation of differences in printing parameters and printing quality
- Impact on attributes of the ceramics

Investigation of the influence of maximum pyrolysis temperature

---

- Preparation of samples with maximum pyrolysis temperatures of 600, 700 & 800 °C
- Measuring pore size distribution, permeability, hydrophilicity, hydrophobicity, carbon- & oxygen content of the prepared samples

Substitution of base polysiloxane with a carbon-rich derivate

---

- Testing of printability and preparation of green bodies of 25, 50, & 75 % amount of substituted PSO
- Pyrolyzing and imaging of samples with selected substitution & maximum pyrolysis temperature
- Measuring pore size distribution, hydrophilicity, hydrophobicity, and carbon content of the selected samples

Evaluation of the adsorption properties of the produced materials

---

- Developing a method for repeatable adsorption measurements
- Measurement of selected promising samples with increasing complexity

3 Theoretical Background

3.1 Porosity

During the processing of materials, the formation of defects is an inherent and unavoidable phenomenon. These defects can manifest in various forms, ranging from zero-dimensional point defects, such as vacancies, interstitials, substitutional atoms, and more, to more complex, three-dimensional bulk defects, including cracks, inclusions, and pores. An overview of how different kinds of point defects can look like is illustrated in Figure 1. While these defects are generally considered undesirable due to their potential to degrade the material's mechanical, thermal, and electrical properties, there are specific instances where the controlled introduction of defects can be advantageous. For example, in the field of semiconductor technology, doping involves the deliberate addition of impurity atoms into a silicon crystal lattice. This process modifies the material's electronic properties, enabling the precise control of conductivity, which is critical for the functionality of electronic devices. [4]

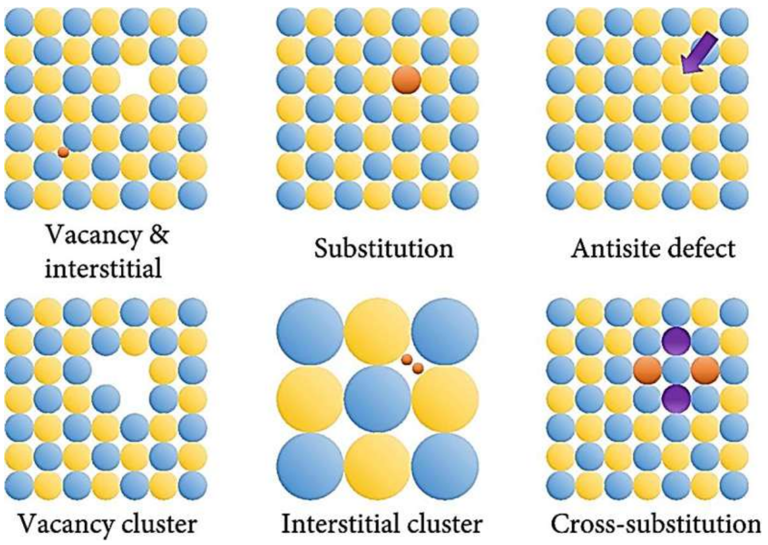

Figure 1: Exemplary overview of different variations of zero-dimensional point defects. [13]

Porosity is another defect that can be strategically utilized to enhance material properties. Unlike point defects or dislocations, porosity involves the presence of voids or pores within a material's structure. Porosity is broadly categorized into two types: closed porosity and open porosity. Closed porosity refers to pores entirely encapsulated within the material, isolated from other pores and the external environment. These closed pores may be filled with gases or liquids or remain as voids, and they generally do not contribute to the material's permeability.

In contrast, open porosity refers to a network of interconnected pores connected or open to the material's surface. This interconnected nature allows for the movement of fluids or gases through the material, making open porosity a critical factor in applications requiring filtration, catalysis, or fluid flow.

Pores can be classified based on connectivity and size, significantly influencing the material's properties and potential applications. The International Union of Pure and Applied Chemistry (IUPAC) has established a standardized classification for pore sizes, dividing them into three distinct categories: micropores, mesopores, and macropores. Micropores are pores with diameters less than 2 nanometers, typically associated with materials that require a high surface area, such as adsorbents and catalysts. Mesopores, with diameters ranging from 2 to 50 nanometers, are often found in materials used for separation processes, where intermediate pore sizes are advantageous. Macropores, with diameters greater than 50 nanometers, are essential in applications that demand high permeability, such as supports in catalysis or scaffolds for tissue engineering. [14]

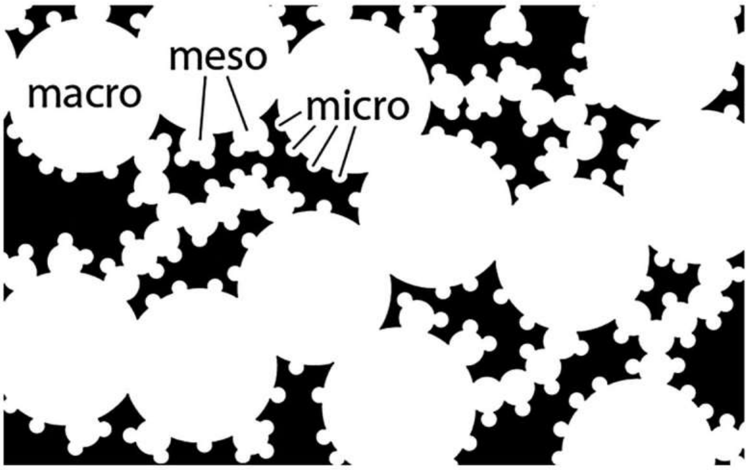

Figure 2: Visual representation of classification of pores and the definition of hierarchical porosity. [15]

When a material exhibits a combination of these pore types interconnected across multiple length scales, it has hierarchical porosity. Hierarchical porosity is particularly valuable in advanced material applications because it combines the benefits of each pore size category, resulting in enhanced performance characteristics. For instance, macropores can facilitate fluid transport in a ceramic material with hierarchical porosity, while mesopores and micropores provide a large surface area for chemical reactions or adsorption processes. This unique combination makes such materials highly suitable for use in catalysis, where the efficiency of the reaction is enhanced by the increased surface area and accessibility provided by the porous structure. Additionally, the ability to tailor the pore structure enables the development of materials for specific applications, such as catalysis, water purification, and gas separation. [9, 16-18]

Processing ceramics with hierarchical porosity requires careful control over the material's structure at multiple scales. Several techniques can be employed to achieve this, ranging from templating methods, which use sacrificial templates to create the desired pore structure, to sol-gel processes, where the formation of the ceramic network is controlled at the molecular level. Among these methods, one of the most promising and versatile approaches is the concept of polymer-derived ceramics (PDCs). This method involves the pyrolysis of pre-ceramic polymers, which undergo chemical transformations at elevated temperatures to form ceramic materials. By selecting appropriate polymer precursors and processing conditions, it is possible to engineer ceramics with tailored hierarchical porosity, enabling the creation of advanced materials with a wide range of functional properties. [19]

In conclusion, while defects in materials are often viewed as detrimental, they can be harnessed and controlled to develop materials with enhanced or entirely new properties. Porosity offers a powerful means of tailoring material characteristics for specific applications, especially when structured hierarchically. The ability to process ceramics with hierarchical porosity through techniques such as polymer-derived ceramics opens new possibilities for material innovation in fields. [5, 6]

3.2 Polymer Derived Ceramics

3.2.1 General Aspects

Conventional ceramics are produced from powders, which are the starting material. The quality and performance of the final ceramic product are highly dependent on the properties of these powders and the processing conditions. Ceramics are often used in extreme conditions, such as for structural components, electronics, and aerospace. Any defects introduced during processing can severely compromise their mechanical, thermal, and electrical properties and lead to critical material failure. Therefore, minimizing defects is an essential objective for ceramic manufacturing.

One primary source of defects is the presence of impurities in the ceramic powder. These can originate from the raw materials or be introduced due to abrasion during the milling and handling. Contaminants can act as sites for defect formation during sintering, in which the ceramic powder is heated to densify and bond the particles together. Defects such as pores, grain boundary phases, and inclusions can lead to microcracking, reducing the strength and durability of the ceramic and leading to critical failure. Additionally, the high sintering temperatures required for traditional ceramics impose significant constraints on the processing techniques that can be employed, limiting the design and complexity of ceramic components. [20]

To overcome these limitations, alternative methods for producing ceramics are explored. One of the most promising alternatives is using preceramic polymers (PCPs). Preceramic polymers are polymers specifically designed to undergo a chemical transformation into ceramics when subjected to high temperatures. This transformation, known as pyrolysis, involves decomposing the polymer's organic components, leaving behind a ceramic material. Ceramics produced through this method are called polymer-derived ceramics (PDCs). Illustrated in Figure 3 are commonly used PCPs as an example.

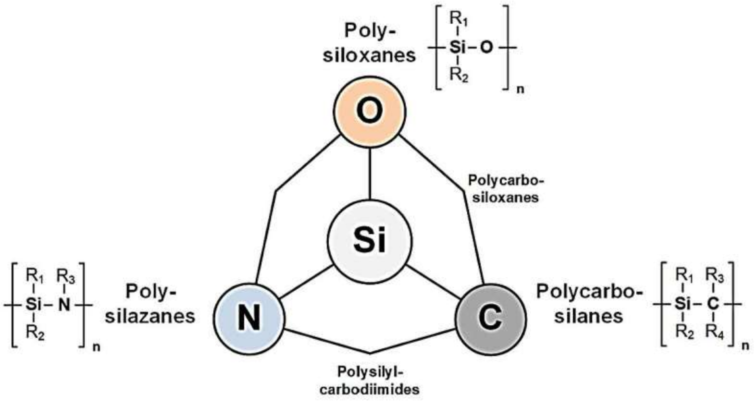

Figure 3: The pillars of preceramic polymers are silicon-based polymers, where the type of heteroatom defines the characteristics and the functional side groups the overall processability. [6]

PDCs offer several advantages over traditional ceramic powders. First, using polymers as a starting material opens a wide range of processing techniques typically associated with plastics, such as injection molding, extrusion, and commercial 3D printing. These techniques allow for the fabrication of complex shapes and structures that would be difficult or impossible to achieve with conventional ceramic powders. This flexibility is precious in advanced manufacturing, where the design freedom and precision offered by polymer processing can lead to the development of novel ceramic components with tailored properties. [6]

The pyrolysis process used to convert preceramic polymers into ceramics occurs at significantly lower temperatures (< 1000 °C) than traditional ceramic sintering (> 1000 °C). This lower processing temperature reduces energy consumption and costs and minimizes the thermal stresses that can lead to warping or cracking during fabrication. Additionally, the lower temperatures expand the range of materials that can be used with the ceramic, such as metal reinforcements, enabling the creation of composite materials with enhanced performance characteristics.

Another significant advantage of using preceramic polymers is achieving high-purity ceramics. Unlike ceramic powders, which can be difficult to purify and are prone to contamination, polymers can be synthesized and purified with a high degree of control before they are converted into ceramics. This high purity level is maintained during pyrolysis, as the controlled decomposition of the polymer ensures that impurities are minimized in the final ceramic material. As a result, PDCs are particularly well-suited for applications where material purity is critical.

Much of the research in the field of preceramic polymers has focused on silicon-containing polymers, such as polysiloxanes, due to their favorable properties. Polysiloxanes are notable for their excellent thermal stability, chemical resistance, and ease of processing. These polymers are often available in oligomeric forms, which can be powders or liquids, further enhancing their processability. During pyrolysis, which occurs within the 300–900 °C temperature range, polysiloxanes transform from an organic polymer to an inorganic ceramic. This transformation involves the evaporation of volatile organic components, leaving behind an amorphous ceramic material that consists primarily of silicon, oxygen, and carbon.

As the temperature increases to approximately 1200 °C, the amorphous ceramic begins to crystallize, forming a more ordered and thermodynamically stable structure without significant mass loss. A carbothermal reduction occurs when the temperature increases further, leading to material degradation. The general reaction mechanism of this polymer-to-ceramic conversion, as represented in Equation 1, illustrates the chemical changes that occur during pyrolysis. This conversion is illustrated in Figure 4.

$$-[SiR_1R_2 - O]_n- \rightarrow Si_xO_yC_z \qquad (1)$$

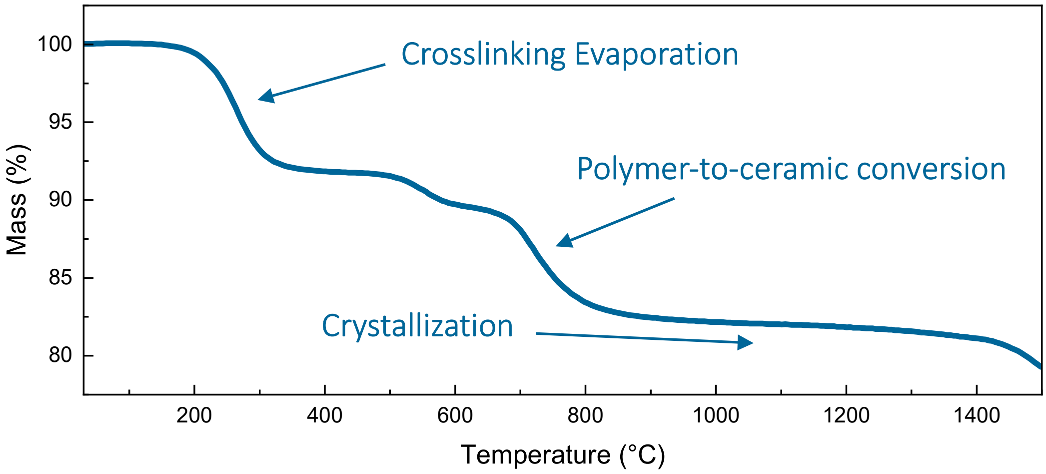

Figure 4: Conversion stages of a preceramic polymer during thermal treatment, illustrated by the mass change of a polysiloxane upon heating in an argon atmosphere.

Preceramic polymers represent a significant advancement in ceramic processing, offering a versatile and efficient alternative to traditional powder-based methods. By leveraging the unique properties of polymers and the lower temperatures required for pyrolysis, it is possible to produce ceramics with enhanced purity, complex shapes, and improved performance characteristics. These advancements open new possibilities for applying ceramics in various industries, from aerospace and electronics to healthcare and environmental technology. [6]

The development of polymer-derived ceramics (PDCs) has led to the emergence of various approaches for fabricating advanced ceramic materials. A significant challenge in traditional ceramic manufacturing is the controlled creation of porosity, which is often difficult to achieve due to the intrinsic properties of ceramic powders and the high sintering temperatures required. However, the PDC approach overcomes this limitation, offering greater flexibility in tailoring the microstructure of ceramics, including the precise control of porosity. [5]

This work focuses on fabricating porous ceramics using a sacrificial templating method enabled by photopolymerization-based additive manufacturing. This method allows for designing and producing complex porous ceramic structures that would be challenging to achieve using conventional ceramic processing techniques.

3.2.2 Photopolymerization-based Additive Manufacturing of PDCs

Various forming processes, such as the sol-gel method, foaming, and additive manufacturing, have been well-established for shaping preceramic polymers (PCPs) into desired structures. Among these, vat photopolymerization using, e.g., LCD, or DLP, has gained attention for its ability to fabricate complex, high-precision ceramic components. This work mainly employs DLP with a digital micromirror device (DMD) to create polymer-derived ceramics with tailored porosity, and therefore, the next section will focus on this additive manufacturing technique.

The setup for DLP-based vat photopolymerization is illustrated in Figure 5. A photocurable resin is deposited within a vat (1), serving as the precursor material. The resin comprises monomers or oligomers that react with light of a specific wavelength. The resin is selectively exposed to light projected from below the vat. The light exposure initiates a photopolymerization reaction, causing the resin to solidify into a defined shape. The photopolymerization process is controlled in a layer-by-layer manner. After each exposure, the building platform (2) moves upwards by the thickness of one layer, typically a few micrometers, allowing a fresh layer of liquid resin to be cured. This process is repeated until the entire green body is fully formed.

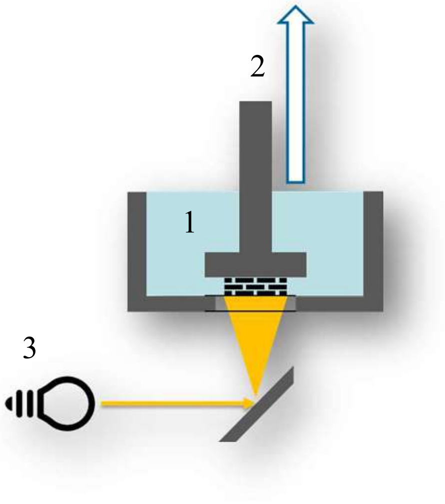

Figure 5: Schematic view of a DMD vat photopolymerization setup.

The digital micromirror device comprises thousands of micromirrors, each capable of tilting to direct light toward or away from the resin surface. This allows for the precise modulation of the light, concentrating it on the areas where curing is wished for. The light not directed at the resin is diverted into a black box, effectively reducing stray light and preventing unintended polymerization in areas meant to remain uncured. This technique offers better control over the photopolymerization process than traditional methods that use masks, e.g., using LCD screens, which can never entirely block all incoming light, leading to potential shadowing effects and defects in the photocured body.

A sacrificial template printing approach is employed to engineer porosity in the final ceramic material. This method involves simultaneously printing two different polymers: one is the preceramic polymer (PCP), which will eventually be converted into the ceramic material, and the other is the sacrificial template polymer designed to be removed later, creating voids and, hence, porosity in the final structure.

The successful implementation of this approach requires that both the oligomeric PCP and the sacrificial monomer be co-dissolved in a single liquid phase before and during the printing process. This ensures that the two polymers are homogeneously mixed and can be printed together. As illustrated in Figure 6A, the two components are mixed in a photopolymerizable solution. Upon exposure to UV light, a phenomenon known as photopolymerization-induced phase separation occurs, where the two polymers solidify into distinct phases. This forms two separate solid phases within the green body, as shown in Figure 6B. The phase of the carbon-based sacrificial polymer decomposes into volatile gases during pyrolysis. Simultaneously, the preceramic polymer converts into a ceramic as shown in Figure 4. The finished ceramic now contains a porous structure, which resembles the phase built up by the sacrificial polymer. [9]

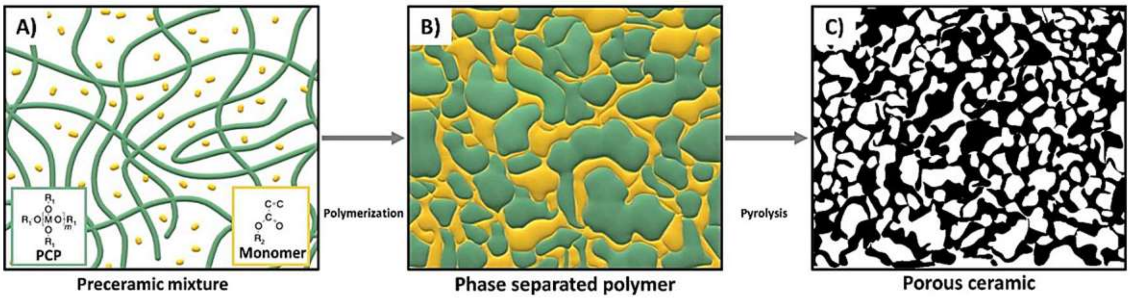

Figure 6: Schematic overview of a phase separation process and the resulting porosity after pyrolysis. In A), two examples of a PCP and a sacrificial monomer can be seen. [9]

The porosity achievable with this technique is in the area of macroporosity, which is generated via the design choice during 3D printing as well as through the photopolymerization-induced phase separation. Although this technique brings forth many advantages, it also has its limitations. A big limitation lies in the size restriction of printable parts. Simple geometries can be printed up to a few centimeters, but crack formation becomes more likely. Also, the higher the geometric complexity of the pyrolyzed parts, the more likely structural failure becomes. The wall thickness should be even across the whole components, so evolving gases can leave the material evenly to decrease the probability of cracks.

In a paper by J. Essmeister, this hierarchically porous ceramic material was first produced. The samples were pyrolyzed at either 600, 700, or 800 °C. The values for specific surface area ranged from 14 to up to 335 $m^2 \cdot g^{-1}$, with an average pore size between 4.6 and 10.7 nm and the median pore diameter in a range from 150 to 425 nm. This material was later functionalized with Nickel as well as Cobalt, Molybdenum, and Lanthanum. There, the values for specific surface area ranged from 175 to 238 m2·g-1, with the average pore size between 3.6 and 6.2 nm and the median pore diameter in a range from 43 to 251 nm, depending on the metal modification for samples pyrolyzed at 700 °C. These modifications were used for catalysis applications. [21]

3.3 Water Purification & Adsorption

3.3.1 General Water Purification Process

Removing contaminations and impurities from water sources is crucial and necessary, as they can potentially harm the environment and humans. It can roughly be categorized in the following steps: Coagulation and flocculation, sedimentation, filtration, disinfection, and optional advanced treatments. These processes are often combined, depending on initial wastewater- and desired outcome quality. The impurity of the initial wastewater depends on its origin. Saltwater, purified to drinking water quality, needs fewer processes than industrial wastewater. There, impurities like organic-, or heavy metal contaminations occur in higher concentrations than in nature. The outcome quality depends on the usage of the treated water. If it is used as drinking water, the health and safety standards are higher and stricter than those used for industrial applications. This chapter will briefly overview the different techniques used and their tasks. [22, 23]

Coagulation and Flocculation is used as a first step. Chemical coagulants are employed, which neutralize the charges of the contaminations. This ensures that the impurities clump together into larger aggregates. Doing so helps the later following step. **Sedimentation** allows the flocs produced in the previous steps to sink into a sedimentation basin. Gravity and time separate the flocks and leave behind clear water above. Doing so reduces the turbidity of the water. During **Filtration**, water passes through different filters, each with its purpose. Sand, gravel, and activated carbon are the most used filter materials. Depending on wastewater impurities, various kinds of filters can be used. These can sieve out, e.g., suspended solids, microorganisms, dyes, or other chemical contaminants. **Disinfection** is necessary to ensure the inactivation of pathogenic microorganisms. Chlorine, ozone, or ultraviolet light are typically used, where chlorine is the most used substance. **Advanced treatments** are often optional and depend on water quality requirements. Activated carbon adsorption is employed when specific organic compounds like dyes must be removed or to filter out taste or odor. Reverse osmosis is mainly used to remove contaminations on the molecular level. Ion exchange is used when removing specific ions, like calcium, magnesium, or nitrate.

3.3.2 Adsorption Techniques & Applications

As advanced treatments, adsorption techniques are commonly used to remove contamination from wastewater. The most used adsorption methods in industry are via activated carbon, ion exchange resins, zeolites, metal-organic frameworks, and biosorption. Via adhesion, atoms, ions, and molecules are bound to the surface of liquids or gases. The material the particles get bound to is called adsorbent, and the particles themselves adsorbate. Adsorption is a purely surface phenomenon often coupled with absorption, which is the intake of particles into the volume of a material. Whether an adsorbent is effective depends on the interaction between the adsorbent and the adsorbate. There are a few key factors that can direct the absorbance efficiency. Those are porosity, surface area, water pH, hydrophilicity, hydrophobicity, temperature, contact time, the concentration of the adsorbate, and regeneration. The surface area and porosity directly relate to the amount of space in which the adsorbent and the adsorbate interact. This increases the capacity of the adsorbent's available sites. If the ionization of a contamination changes with the pH value of water, so does the interaction between adsorbent and adsorbate. The same is true for the hydrophilicity and hydrophobicity of the adsorbent. Due to being mostly exothermic, absorbance reactions can be more efficient at lower temperatures. The contact time must be sufficient for the adsorbate to react with the surface of the adsorbent. This can be done via a high dwell time of the contamination or by refluxing the water, e.g., via a tubular reactor. If the adsorbate concentration is very high, the surface of the adsorbent gets saturated quickly, decreasing efficiency. Some adsorbents can be regenerated. This can be done via thermal or chemical treatment. The amount and efficiency of the adsorbent after many regeneration cycles are crucial. When the efficiency of the adsorbent gets below a certain threshold, it gets disposed of. [22, 23]

This work uses the molecule methylene blue (MB) as a model molecule. It is a widely used dye, which is suitable to simulate organic substances and is easily traceable due to its strong blue color. The chemical structure of MB can be seen in Figure 7.

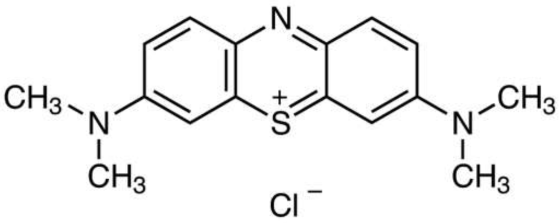

Figure 7: Chemical structure of the molecule methylene blue, mainly used as a dye.

3.3.3 Use of PDCs as adsorbent for removal of organic contaminants

Polymer-derived ceramics have previously been investigated with respect to their adsorption capabilities for organic dyes. These investigations produced SiOC or SiC ceramic materials through preceramic polymers. However, the combination of the application of dye adsorption and additive-manufactured ceramic bodies has not yet been done. Table 1 gives an overview of works comparing shaping, the experimental setup of the dye measurements, and the results of said experiments. Research concerning degradation processes during dye adsorption is excluded due to their difference in mechanisms. [10-12, 24-28]

The literature on this field is limited and often specific to certain aspects of the adsorption process, e.g., adsorption kinetics, degradation processes, or adsorption of particular molecules. Dyes were mostly used as model molecules due to their visibility in solution and ease of measurement via UV/VIS spectrometry. A work by J. Pan reported on the adsorption of the antibiotic ciprofloxacin (CIP). The samples in the papers were either milled as powder or shaped into aerogels and directly put into the dye solution in batch processes. No efforts were made to simulate continuous or reactor conditions.

Additionally, to the knowledge of the author, no work has been done on the evaluation of PDCs shaped by additive manufacturing for this purpose.

In conclusion, a polymer-derived ceramic, produced via additive manufacturing, shaped to fit into a continuous setup, would prove to be an innovative and novel topic in the field of dye adsorption.

Table 1: Comparison of different research papers regarding shaping, experimental setup, and capacity measured for dye adsorption. **Different pyrolysis temperatures, concentration of additives, or post-treatment of the material.*

Shaping	Experimental setup	Dye used	Dye concentration ($mg \cdot L^{-1}$)	Capacity q_t ($mg \cdot g^{-1}$)	Source
SiOC Aerogel	Powder stirring in a rotary shaker	MB	1 / 100	0.167 / 15.7	[10]
SiOC Aerogel	Powder stirring in a rotary shaker	MB	100	44.2	[11]
SiOC Powder	Powder stirring in a rotary shaker	MB	25	49.26 / 104.27*	[12]
SiOC Powder	Powder stirring in a rotary shaker	Rhodamine B (RB)	25	49.38 / 110.74*	[12]
SiOC Powder	Powder stirring in a rotary shaker	Crystal Violet (CV)	25	49.47 / 185.87*	[12]
SiOC Powder	Powder stirring in a rotary shaker	MB	25	69.17 / 111.58 / 146.77*	[26]
Ni/SiOC Powder	Powder stirring via ultrasonic bath	Acid fuchsin (AF)	200	129.8 / 180.32*	[27]
SiOC Powder	Powder stirring in a rotary shaker	CIP	10	85.4 – 107.57*	[28]

4 Experimental

4.1 Materials & General Processing

All materials used in this work are given in Table 2.

Table 2: Recording of the material used in this work.

Name	**Abb.**	**Company; Purity**	**Usage**
Methylene blue	MB	Merck; -	Adsorbent
n-Heptane	-	Sigma Aldrich; 99 %	Solvent
Phenylbis (2,4,6-trimethylbenzoyl)	BAPO	Rahn; 97 %	Photoinitiator
Silres MK Polysilsesquioxane	PSO1	Wacker-Chemie, -	Preceramic Polymer
Silres H44 Polysilsesquioxane	PSO2	Wacker-Chemie, -	Preceramic Polymer
Tetraethyl orthosilicate	TEOS	Sigma Aldrich; 99 %	Solubilizing agent
Trimethylolpropane trimethacrylate	TMPTMA	TCI; 90 %	Monomer
Tripropyleneglycol methylether	TPM	Sigma Aldrich; 97.5 %	Solvent

4.1.1 Resin Preparation

The resin utilized for vat photopolymerization was prepared consistently using a standardized procedure throughout the work. This formulation was initially developed in a previous work of A. Fuchsberger [29]. PSO (white powder, 22 wt.%), as either PSO1, PSO2, or a mixture thereof, was weighed and transferred into a brown glass flask of appropriate volume. TPM (liquid, 22 wt.%), TEOS (liquid, 12 wt.%), and TMPTMA (liquid, 44 wt.%) were sequentially added directly into the flask in the specified order. The mixture was stirred using a magnetic stirrer until complete dissolution. Before photopolymerization, BAPO (white powder, 1 wt.% added to the overall weight of the mixture) was added and dissolved using an ultrasonic bath for ten minutes. The final weight of the formulation was adjusted to the required amount of the material for printing.

4.1.2 Additive Manufacturing (AM)

For the design of simple shapes and modification of existing print files and their parameter, the LycheeSlicer software was used. The green bodies were printed using two different 3D printers (Anycubic Mono 4k, an LCD-based printer, as well as Anycubic Photon D2, a DLP-based printer). These were used and compared based on printing quality and speed. Table 4 provides an overview of the adjustable parameters for the printing process, which were adopted from a previous work of J. Essmeister [9]. The layer thickness was kept at 25 µm for all experiments. The exposure intensities of the light source for each printer were measured and quantified using an Ocean Optics spectrometer. The printing parameter remained constant, except for the exposure time, which was optimized through a series of exposure tests. Post-printing, the green bodies were washed in TPM and dried at room temperature. An overview of the printed sample, their geometry, and geometric dimensions is given in Table 3. The specific geometrical features of the samples for each characterization method are given in each of the sections.

Table 3: Overview of the different geometric shapes and their dimensions printed by the Mono 4K and the Photon printers.

Sample description	Geometric shape	Diameter x Height (mm x mm)
Cylinder	Cylindrical	Between 5 x 5 and 10 x 25
Tube	Cylinder with a cylindric hole	10 x 10 with a 5 x 10 hole
Gyroid	Cylindrical gyroid	10 x 10
Honeycomb	Cylinder with hexagonal lattice holes	10 x 10
Wurtzite	Cylindrical wurtzite structure with hexagonal holes	10 x 10

The exposure intensity was measured directly on the printing surface of the 3D printer. Measurements were conducted at nine distinct points across the printing surface to account for any variations in intensity. The layout of these measurement points on the printing surface is depicted in Figure 8.

Exposure tests were performed by applying a few drops of resin formulation and exposing it on the printing screen of the 3D printer for a specified duration. The resulting solidified material was measured for thickness using a caliper, and the minimum exposure time required to achieve 25 µm thickness was determined.

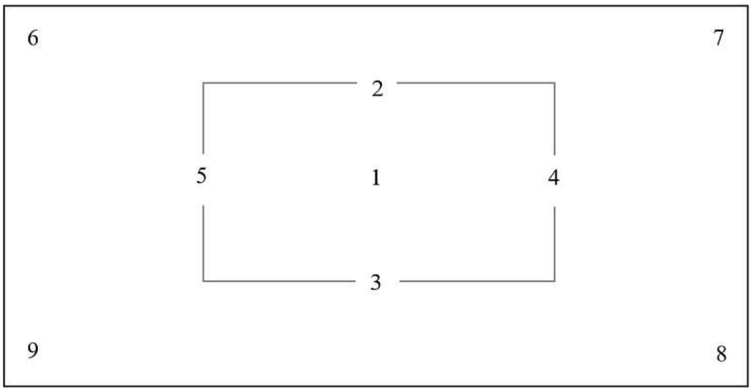

Figure 8: Exposure Intensity setup, each number representing one measurement point on the printing surface (depicted as the outer rectangle). The inner rectangle represents the outline of the vat position.

Table 4: Printing parameters for the vat photopolymerization 3D printers.

Printing parameter	
Wavelength (nm)	405
Exposure intensity (mW·cm^{-2})	variable
Bottom layer count	5
Layer height (µm)	25
Light-off delay (s)	0.5
Bottom lift speed (mm min^{-1})	60
Lifting speed (mm min^{-1})	60
Bottom retract speed (mm min^{-1})	180
Retract speed (mm min^{-1})	180

4.1.3 Pyrolytic Conversion

The printed green bodies were measured for length and width using a caliper and weighed using a precision scale. Up to 20 samples were placed on a crucible and positioned at the center of a tube furnace. The furnace (Carbolite HZS 12/600, 1100 °C split tube 3-zone furnace), was sealed, and a vacuum was applied for five minutes, followed by flushing with argon gas (Argon purity: 99.995 %). This cycle was repeated twice to ensure an inert atmosphere. A continuous gas flow of 0.5 l·min^{-1} of argon was maintained throughout the pyrolysis process. The furnace was activated, and the samples were subjected to a programmed temperature program, as illustrated in Figure 9. The maximum pyrolysis temperature was varied between 600, 700, and 800 °C. After cooling down to room temperature, the samples were re-measured for length and width and re-weighed to determine the linear shrinkage and the ceramic yield of the samples, respectively.

Ceramic yield is the percent of mass that remains after the pyrolysis process. For its calculation, a sample's mass (m) before and after pyrolysis must be measured, indicated with subscripted i and f, which stand for initial and final. Equation 2 was used for calculating the ceramic yield (Y_C) of selected samples. For each value, five samples were measured.

$$Y_C = \frac{m_f}{m_i} \cdot 100 \tag{2}$$

The **linear shrinkage** of a sample determines the percentage of linear dimension lost during the pyrolysis process. Therefore, the length and width of cylindric bodies in the xy- and z-direction were measured before and after the pyrolysis process. Equation 3 calculates the selected samples' linear shrinkage (s_l). For each value, five samples were measured.

$$s_l = 100 - (100 \cdot \frac{xy/z_f}{xy/z_i}) \tag{3}$$

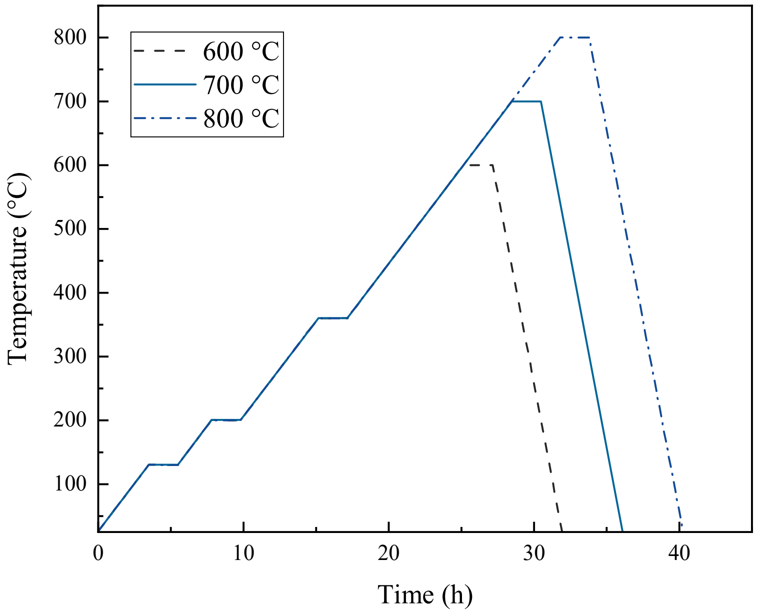

Figure 9: Temperature program for the pyrolytic conversion of preceramic polymer green bodies. The maximum pyrolysis temperature was varied between 600, 700, and 800 °C.

4.2 Characterization

4.2.1 Porosity & Structural Features

Mercury Intrusion Porosimetry (ThermoFisher Pascal 140/440) is an analytical technique to characterize porous materials pore size distribution and open porosity. Depending on porosity, a cylindrical monolithic sample, typically 50 to 100 mg and 5 x 10 mm in length x width, is weighted and placed into a specially designed glass flask called a dilatometer. The dilatometer is then inserted into the low-pressure chamber of the ThermoFisher Pascal 140. After applying a vacuum, a specified amount of mercury is introduced into the dilatometer. The atmospheric pressure is then gradually restored, and the pressure of the surrounding air is continuously monitored. The dilatometer contains the mercury, and the sample is weighted and transferred into the high-pressure device. Pressure is systematically increased from atmospheric levels to 200 – 400 MPa maximum. Low-pressure and high-pressure are combined for a comprehensive analysis.

Although the software calculates the data, doing this task manually with the help of the Washburn-Equation (Equation 4) for cylindrical pores is also possible. There, P_L is the pressure of the liquid, P_G is the pressure of the gas, σ is the surface tension of the liquid, θ is the contact angle of the liquid, and D_P is the pore diameter. [30]

$$P_L - P_G = -\frac{4\sigma \cdot cos\theta}{D_p} \tag{4}$$

This equation can be simplified for the application of the mercury intrusion system. P_G can be set to zero through the use of a vacuum. The contact angle of mercury and the surface tension in a vacuum are known and given as numerical values. The exact values are unknown in this case, so they will be defined as x. If the equation is written for D_P as the unknown, Equation 5 is generated. With this equation, only the pressure recordings of the measurements are required to calculate the pore size distribution.

$$D_P = \frac{x}{P_L} \tag{5}$$

Scanning Electron Microscopy (SEM) is a high-resolution imaging technique capable of resolving features to a few micrometers. This method provides detailed information about pore size distribution, morphology, and the quality of the printing process by examining the surface and the cross-section of monolithic samples. For imaging, high vacuum mode combined with secondary electron detection was used. The pyrolyzed samples were sputtered-coated with a thin layer of gold (AU). All images were captured using a field emission gun electron source (FEG-SEM, FEI Quanta 2050 FEG).

3D-Microscopy (Keyence VHX-5000) was utilized to image samples on a macroscopic scale. This technique was used to monitor topological features visually and to measure geometric dimensions with higher precision than achievable with a caliper.

Permeability is a macroscopic feature of the material, which describes the ease of laminar air flow through porous material. A cylindrical monolith was measured for length and diameter with a length x width of 3.5 x 8.5 mm, and the ambient temperature was recorded using a thermometer. The sample was encased in a shrink tube and heated with a heat gun to ensure a snug fit around the sample. The tube was tightly clamped into the measurement setup, as illustrated in Figure 10. After verifying for air leaks, pressurized air was incrementally increased by 0.2 bar. The downstream pressure (p2) and the airflow rate (Q) were recorded at each pressure increment. The airflow was quantified using a bubble flow meter, where the time taken for a soap bubble to rise through a defined volume was measured.

To calculate the permeability constants, the Darcian permeability k_1 (m^2), and the non-Darcian permeability k_2 (m), the Forchheimer equation for compressible media was used (Equation 10), where P_i is the absolute fluid pressure at the medium inlet, P_o is the absolute fluid pressure at the medium outlet, P is the absolute fluid pressure at which v_s, μ and ρ are measured or calculated, L is the medium thickness along the flow direction, μ is the absolute viscosity, ρ is the density of the fluid and v_s is the superficial fluid velocity, defined by $v_s = Q/_A$. Q is the volumetric flow rate and A is the exposed surface area of the porous medium perpendicular to the flow direction.

$$\frac{P_i^2 - P_o^2}{2 \cdot P \cdot L} = \frac{\mu}{k_1} v_s + \frac{\rho}{k_2} v_s^2 \tag{6}$$

The Forchheimer Equation can be solved by bringing it into the form of $y=ax+bx^2$, which was already done in Equation 6. There, y is put together of the first half of the equation, which consists of the experimental data recorded during the permeability experiments, and x is the velocity μ_s, which was also recorded. The fitted constants a and b are then calculated. The permeability parameters can then be calculated by $k_1=\mu/a$ and $k_2=\rho/b$. [31, 32]

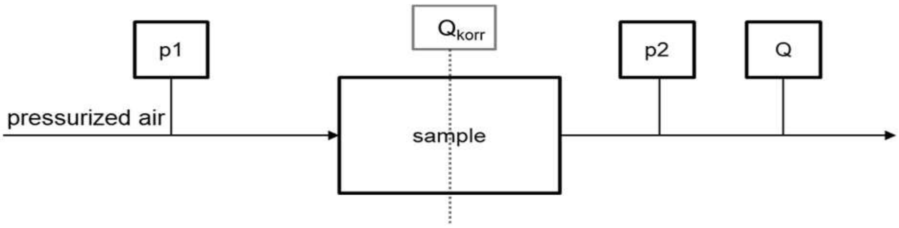

Figure 10: Scheme of the measurement setup for permeability tests.

4.2.2 Chemical Composition

Carbon was quantified by the hot gas extraction technique by combusting a few milligrams of powdered sample in an oxidizing atmosphere. The resulting CO_2 gets detected and measured using an infrared cell. **Oxygen** was quantified via the inert gas fusion method. The oxygen in the powder reacts with the carbon in the crucible and forms CO_2, which can be detected and measured with an infrared cell. Carbon measurements were performed using a LECO CS230, while oxygen was analyzed with a LECO TC400. Both Measurements and calibration with standard reference material were done via triplicate measurements. The samples were placed in ceramic crucibles for carbon analysis, and tungsten chips were added to act as an ignition accelerator. Oxygen samples were enclosed in tin capsules, sealed to minimize air presence, and dispensed into graphite crucibles for analysis.

To calculate the amount of hydrogen and silicon combined, Equation 7 was used.

$$\%_{Si+H} = 100 - \%_{C} - \%_{O} \tag{7}$$

Thermogravimetric - & Differential Thermal Analysis (TGA & DTA) were conducted simultaneously using a NETSCH STA 449 C to assess mass loss and exothermic/endothermic transitions during thermal treatment. A sample of 50 – 100 mg of powder was weighted into a ceramic crucible and placed inside the measurement chamber. The chamber was evacuated and purged with argon three times before starting the analysis. The measurement was performed under an argon flow of 50 $ml \cdot min^{-1}$. The chamber was heated at a constant rate of 5 $K \cdot min^{-1}$ until a final temperature of 1500 °C was reached. This analysis was used to evaluate the polymer-to-ceramic conversion of the PSO1, PSO2, and their mixtures and to study their impact on mass loss and conversion behavior.

4.2.3 Surface Characterization

Hydrophilicity & Hydrophobicity were assessed by exposing samples as a powder or monolith gyroids, with length x width of 10 x 10 mm measured as green bodies, to the saturated vapor of water and n-heptane, following a methodology previously reported by Szoldatits et al. [33]. The samples were dried in an oven at 110 °C until a constant weight was achieved. Water and n-heptane each were placed in separate crystallizing dishes at the bottom of the individual desiccator. A heating mat, maintained at 25 °C, was positioned beneath the desiccators to ensure a stable vapor-liquid equilibrium. The dried samples were placed into the desiccators and weighed regularly until no further weight change was observed. The amount of solvent adsorbed was calculated with Equation 8 and the hydrophilicity was calculated with Equation 9. [33]

$$Amount\ adsorbed = \frac{m_f - m_i}{m_i} \cdot 100 \tag{8}$$

$$Ratio\ adsorbed = \frac{H_2O\ adsorbed}{n - Heptane\ adsorbed} \tag{9}$$

Adsorption experiments were carried out by exposing monolithic samples to diluted methylene blue solutions and subsequently measuring the concentration of the solution using UV/VIS spectroscopy (IMPLEN NanoPhotometer). These samples were either in a shape of a tube with 10 x 10 mm in length x width and a hole in the center with a diameter of 5 mm, or gyroids with a length x width of 10 x 10 mm (measurements were performed on the green bodies due to different shrinkage behavior of the used material). A stock solution was prepared by dissolving one gram of methylene blue in one liter of distilled water, diluted to a concentration of 0.1 $mg \cdot l^{-1}$. This dilution series was analyzed using a UV/VIS spectrometer to establish a calibration curve within a linear range, enabling the determination of unknown methylene blue concentrations in water.

For the adsorption experiment, 100 ml of a specified concentration of methylene blue solution was placed in a beaker, and its concentration was measured via UV/VIS spectroscopy. A magnetic stirring bar was added, and the beaker was placed on a magnetic stirrer set at 250 rpm. A pyrolyzed monolithic sample was enclosed in a shrinking tube and heated with a heat gun. The tube was then connected to a peristaltic pump, which circulated the solution away from the beaker, through the sample, and back into the beaker with a varying flow rate of either 0.5 or 3 $ml \cdot s^{-1}$ for 24 hours. After the exposure period, the solution was reanalyzed using UV/VIS spectroscopy to determine the change in concentration. A picture of the experimental setup is shown in Figure 11.

The value of the capacity q_t is used to evaluate the efficiency of adsorbent material. The higher the value of q_t the better the adsorbent material. This can be calculated with Equation 10, where c_i is the initial concentration, c_f is the final concentration, V is the volume of diluted adsorbate in water, and m_{ads} is the mass of adsorbent used. The absorbance of the dye in percent (R_{ads}) was also calculated with Equation 11 to evaluate the effectiveness of complete dye removal.

$$q_t = \frac{(c_f - c_i) \cdot V}{m_{ads}} \tag{10}$$

$$R_{asd} = \frac{c_i - c_f}{c_i} \cdot 100 \tag{11}$$

Figure 11: Setup for the adsorption experiment. A methylene blue solution is pumped away from the beaker, through the sample, and back into the beaker. The flow rate is set via the pump controller (grey).

5 Results & Discussion

5.1 General Processing

Exposure intensity tests, exposure tests, and microscopic imaging were conducted to oversee the printing of the green bodies. TGA, microscopic imaging, and FEG-SEM were also carried out to supervise the pyrolysis process. Unless otherwise stated, only PSO1 was used as the preceramic polymer in all samples.

5.1.1 Additive Manufacturing

The exposure intensity of the employed 3D printers was measured. There, the intensity of the Mono printer could be chosen between values of 0 – 100 %. 25, 50, 75, and 100 % were selected to be measured. The results can be found in Table 5.

Table 5: Results of the exposure intensity tests for the Photon- and Mono printer.

	Photon	Mono @ 25 %	Mono @ 50 %	Mono @ 75 %	Mono @ 100 %
Exposure intensity (mW·cm^{-2})	1.33 ± 0.04	0.95 ± 0.10	1.35 ± 0.23	1.59 ± 0.16	1.94 ± 0.27

The Mono printer at 100 % intensity shows the highest value, indicating faster printing times. The Photon printer shows the lowest deviation across all measurement points (shown in Table A1), meaning the printed green bodies can be expected to exhibit comparable properties independent of the placement within the printing area.

The exposure tests were conducted to measure how much time one layer needs to be 25 µm in thickness. The photon and Mono printers were tested at 25, 50, 75, and 100 % intensity. The results can be found in Table 6 and depicted in Figure 12.

Table 6: Results of the exposure tests for the Photon- and Mono printers. The exposure time given is the time needed for a layer of 25 µm in thickness to be formed.

	Photon	Mono @ 25 %	Mono @ 50 %	Mono @ 75 %	Mono @ 100 %
Exposure time (s)	15	20	15	12	9

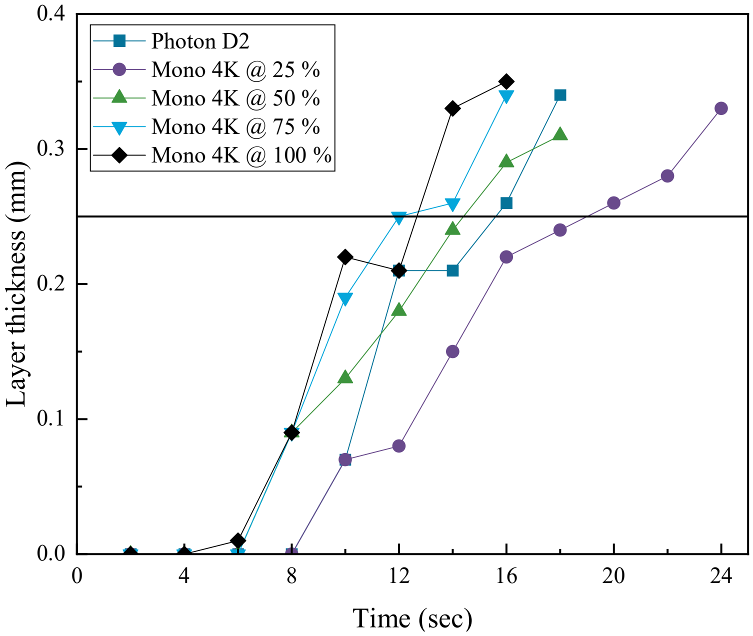

Figure 12: Time-dependent exposure tests to determine the time needed for a layer to reach 25 µm in thickness (marked with the horizontal line in the graph).

With longer exposure times, thicker layers will take shape. For the Mono 4K printer at 100 % exposure intensity a decrease in layer thickness with increasing time can be seen. The cause for this is probably a formation of air bubbles, which distorted the measurement of layer thickness.

Due to their similarities of low exposure intensity derivation and moderate printing time, the Photon printer and the Mono printer at 25 % were chosen to produce polymer-derived ceramics for this thesis.

To protocol the process and the quality of the green bodies, **microscopic images** were taken. An example of a complex gyroid-shaped sample can be seen in Figure 13.

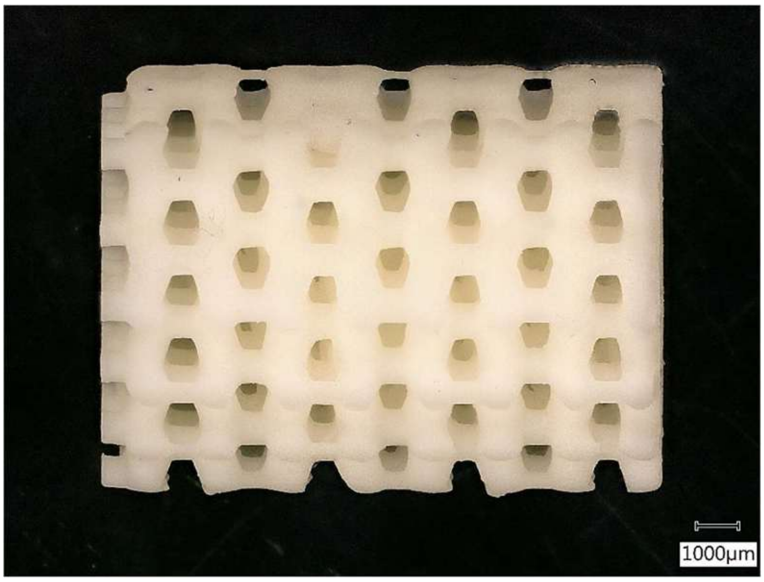

Figure 13: 3D printed preceramic polymer shaped as a complex gyroid, printed with the Photon printer with an exposure time of 15 sec and a layer thickness of 25 µm per layer.

Complex shapes like a honeycomb structure or a gyroid can be obtained. Most defects appear on the outside of the samples, resulting from the handling of the samples. The higher the complexity, the easier these defects occur during cleaning, moving, and measuring. But overall, the samples, with care, are easily handled and structural integral.

5.1.1 Pyrolysis processing

To assess the pyrolysis process, **TGA** of the powder and the resin for 3D printing of PSO1 were carried out. These measurements were conducted to validate the established temperature program of J. Essmeister, illustrated in Figure 9. The results are depicted in Figure 14, where the dwell times of the temperature program are indicated as black vertical lines. [21]

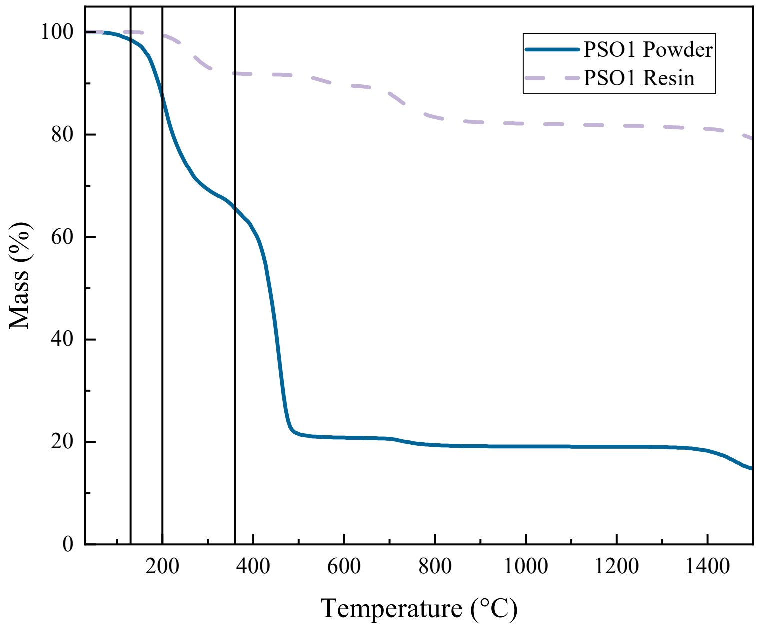

Figure 14: TGA measurement of PSO1 in powder form and mixed as a resin, ready for 3D printing. The dwell times of the later pyrolysis program are indicated in the diagram as black vertical lines.

At the first dwell segment at 130 °C, remains of the solvent are evaporated, which originates from the 3D printing and following washing of the samples with TPM. At 200 °C and 360 °C, respectively, a high amount of mass is lost. To prevent cracks from forming, the dwell times appear to be well-suited. Overall, this temperature program can be used as it is and is applicable to this process.

To protocol the process and the quality of the pyrolyzed ceramics, **microscopic images** of the pyrolyzed parts were taken. An example of a complex gyroid-shaped sample can be seen in Figure 15.

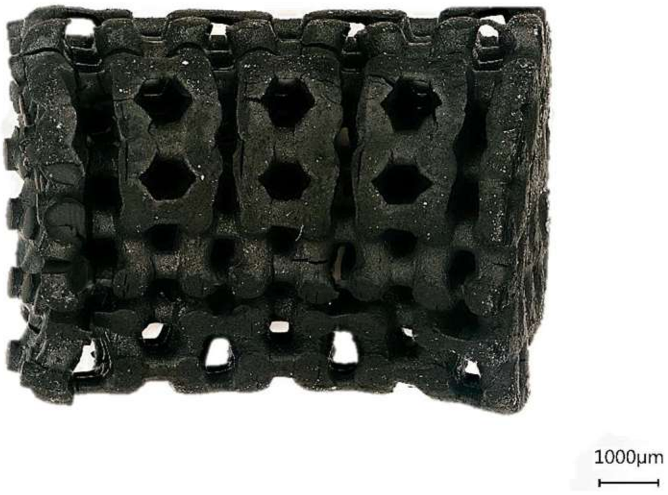

Figure 15: Polymer-derived SiOC ceramic printed with the Photon printer and pyrolyzed at 700 °C in the shape of a complex gyroid. The sample was printed with the Photon printer with an exposure time of 15 sec and a layer thickness of 25 µm per layer.

Overall, the structural integrity of the sample is preserved, compared to Figure 13, but a curvature can be recognized on the horizontal sides. This arises when the linear shrinkage during pyrolysis is anisotropic. The cause can be manifold; the preceramic polymer could not be distributed evenly during 3D printing or for other process-related reasons. The behavior of the anisotropic shrinkage will be further investigated in Chapter 5.3.

FEG-SEM images of the microstructure were taken to validate the creation of a hierarchically porous ceramic. The layered structure of a sample fragment, pyrolyzed at 700 °C, was captured in different magnifications, as shown in Figure 16.

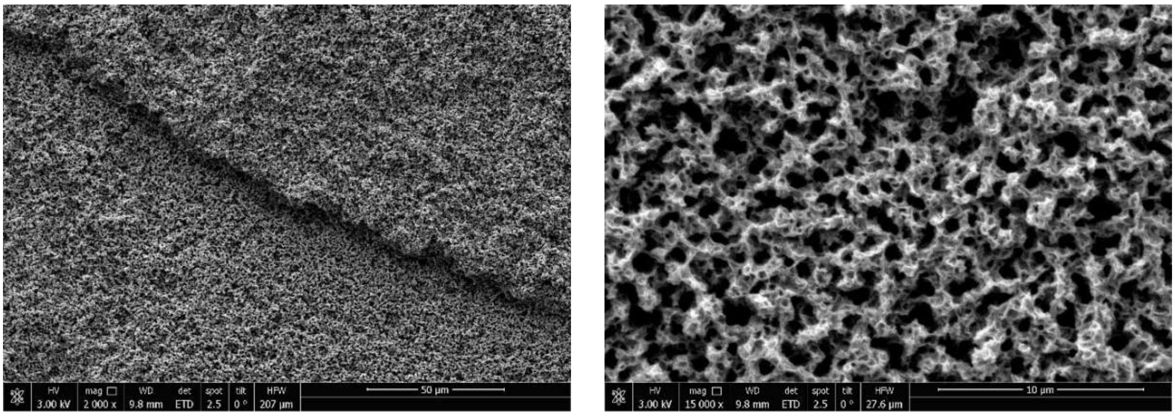

Figure 16: FEG-SEM images of a layer transition of a sample, pyrolyzed at 700 °C, in two different resolutions. The passing of one layer to the next can be seen on the left. On the right, the microstructure of a layer can be seen with pores reaching the sub µm region.

Even after pyrolysis, the layered structure of the 3D printing process can be seen clearly. At higher resolutions, a continuously distributed porosity can be observed.

5.2 Ceramic Yield & Linear Shrinkage

Samples with a pyrolysis temperature of 600 °C, 700 °C, and 800 °C printed on the Anycubic Photon D2 (Photon) and samples with a pyrolysis temperature of 700 °C printed on the Anycubic Mono 4K (Mono) as a reference are compared in Table 7. The ceramic yield increases at higher pyrolysis temperatures with samples made with the Photon printer. This can also be seen in the linear shrinkage in the xy- & y-direction.

Table 7: Ceramic Yield and linear shrinkage in xy- and z-direction of cylindrical specimen of PSO1 after pyrolysis in Ar atmosphere at 600 °C, 700 °C, and 800 °C.

	Photon @ 600 °C	Photon @ 700 °C	Photon @ 800 °C	Mono @ 700 °C
Ceramic yield (%)	18.1 ± 0.5	18.2 ± 0.1	19.8 ± 0.3	19.6 ± 0.7
Lin. shrinkage xy (%)	19.5 ± 1.1	27.5 ± 1.6	27.8 ± 1.0	26.1 ± 1.3
Lin. shrinkage z (%)	18.1 ± 0.5	30.2 ± 1.3	32.1 ± 1.2	28.3 ± 0.9

Through the setup of the tube furnace, a trend of increasing ceramic yield, as seen with the samples of the Photon printer, with increasing pyrolysis temperature, is unlikely. The argon flow passes through the tube and transports away the emerging gases during pyrolysis. So, with rising temperatures, the ceramic yield typically goes down. The varying amounts of TPM can explain the trend seen in Table 7 on the printed parts. Depending on the duration between printing and pyrolysis, the parts can be dry or other factors (humidity, room temperature, amount of wash-TPM used, etc.…). More TPM would increase the initial mass and decrease the resulting ceramic yield, and vice versa. Overall, ceramic yields of 18 – 20 % were observed independent of the selected printer or temperature in the inspected range.

The linear shrinkage in the xy- & z-direction of the samples produced with the Photon printer increases with increasing pyrolysis temperature. The printing direction, illustrated in Figure 17, which is the z-direction, influences the shrinkage of the samples during pyrolysis differently than the shrinkage in the xy-plane. One reason can be that the polymer network in the layer is more intertwined, while between layers, the interconnection is interrupted. During the forming of the amorphous ceramic, the inorganic molecules are closer to each other in a layer than on the layer interface. This would lead to lower shrinkage in a layer and more between two layers. So, for samples produced at 600 °C pyrolysis temperature, where this polymer-to-ceramic conversion begins to take place, the shrinkage in the z-direction would not yet be as high as for samples, produced at higher pyrolysis temperatures.

While preparing different samples, some samples showed a higher shrinkage at one end of the pyrolyzed body than on the other. This anisotropic shrinkage was of conical form.

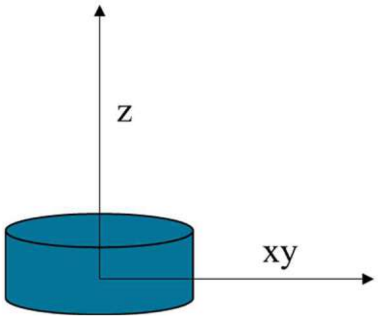

Figure 17: 3D printed green body (in blue) with displayed printing direction (z) and layer direction (xy).

5.3 Conical Shrinkage

The conical shrinkage was investigated via different approaches (named A to F), summarized in Table 8. All approaches were performed with comparable printing bodies, which are cylinders, and pyrolysis temperature at 700 °C and measured in triplicates. For comparison, approach A was done following the standard procedure. Approach B was conducted to investigate if the components' segregation occurs at some point during printing. The tendency for either PSO or the sacrificial monomer to be consumed out of the resin more than the other during printing was checked in approach C. The hypothesis is that if components are available in excess, then conical shrinkage should not occur. Approaches D – F were chosen to investigate if this conical shrinkage is more pronounced at low resin availability.

Table 8: Description of different approaches to gain information on the cause of conical shrinkage.

	Approach description
A	Print with standard procedure.
B	Interruption of the print every 15 minutes and homogenization of the resin in the vat by hand
C	Available resin in the vat was doubled
D	50 % of resin printed, which was available in the vat
E	70 % of resin printed, which was available in the vat
F	90 % of resin printed, which was available in the vat

A metric to quantify conical shrinkage is introduced with Δw (%). It is calculated according to Equation 12 and describes the difference of the width of a pyrolyzed cylindrical sample measured at the top end of the sample in the z-direction, indicated with a subscripted t, and at the bottom, indicated with a subscripted b.

$$\Delta w = \frac{width_t - width_b}{width_b} \cdot 100 \tag{12}$$

The investigation results can be found in Table 9 are illustrated in Figure 18. The standard procedure resulted in a Δw value of 1.95 ± 0.72 %. Approach B, where the photopolymerization was stopped every 15 minutes to homogenize the resin, resulted in a similar range with a higher deviation with a value of 2.36 ± 1.27 %. Out of all approaches, the lowest value was achieved by approach C, where the amount of resin was doubled. It reached a Δw of 0.84 ± 0.64 %. The highest measured value was of approach F with a Δw of 19.91 ± 2.19 %.

Table 9: Results of the investigation of the occurrence of conical shrinkage for approaches A – F.

	A	B	C	D	E	F
Δw (%)	1.95 ± 0.72	2,36 ± 1.27	0.84 ± 0.64	5.56 ± 0.63	9.35 ± 3.63	19.91 ± 2.19

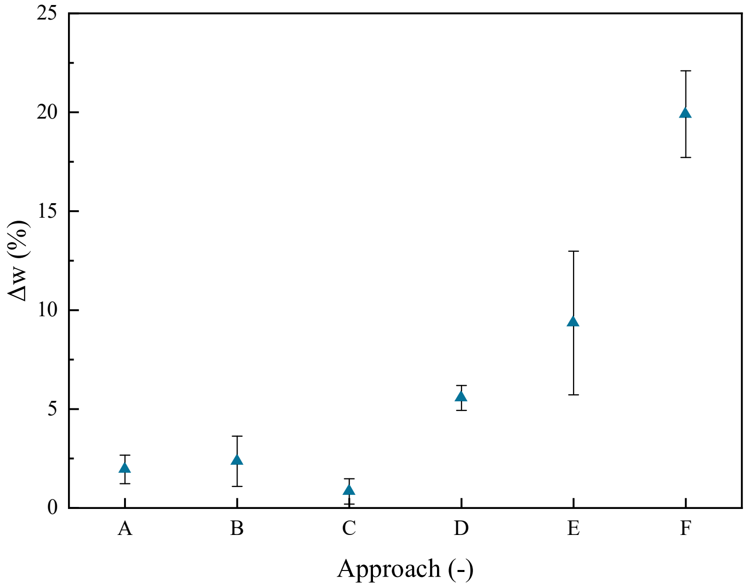

Figure 18: Results of the investigation of the occurrence of conical shrinkage for approaches A – F.

With approach A as a comparison, approach B worsens the occurrence of the conical shrinkage while providing double the amount of resin (approach C) reduces it. So, segregation of the resin did not occur, but the higher availability of resin seemed to counteract this anisotropic behavior. This indicates that some components are more likely to be incorporated into the printed structure than others. For clarification purposes, approaches D – F were carried out. The results of these approaches seem to confirm this behavior. A new variable represents the amount of resin printed into green bodies from the total available resin for the 3D print. It is calculated with the help of Equation 13 for all approaches (approach B was not calculated) and is ordered in ascending amounts of resin printed and illustrated in Figure 19. The amount of resin printed seems to significantly impact the occurrence and extent of conical shrinkage. With the observation that higher shrinkage always occurs in part regions that had been printed last, the hypothesis that some resin component has a higher affinity to be consumed during printing than others seems to hold. To expand on it with the gained data, it can be assumed that the component with the higher affinity is the preceramic polymer. The reason for this assumption is that higher shrinkage occurs when the amount of PSO in the green body is lower, and the amount of sacrificial monomer is higher.

Overall, to counteract the conical shrinkage, the maximum relative amount of resin used during a giving print run was limited to 20 % of the starting amount.

$$Resin\ printed = \frac{total\ mass\ of\ printed\ green\ bodies}{available\ amount\ of\ resin} \cdot 100 \tag{13}$$

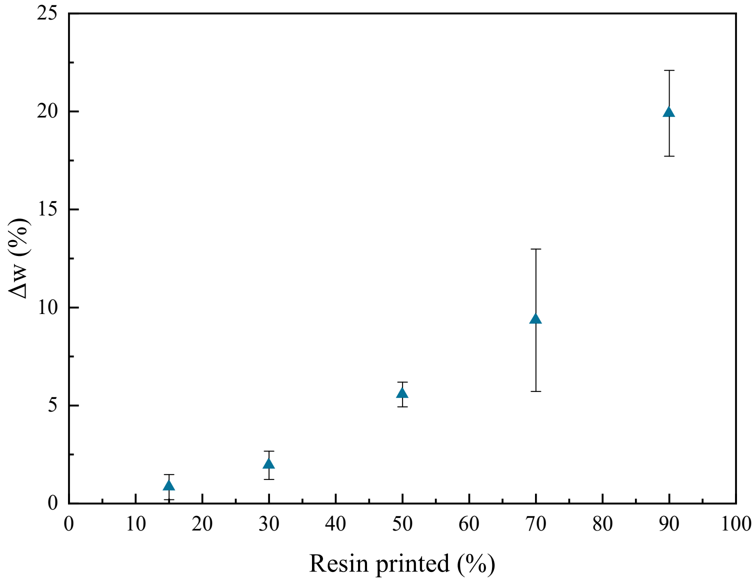

Figure 19: Results of the investigation of the occurrence of conical shrinkage, ordered by the relative amount of resin used based on the initial amount of resin.

5.4 Chemical & Surface Properties

5.4.1 Carbon & Oxygen Content

The respective equipment software directly gave the values for carbon and oxygen. Samples with a pyrolysis temperature of 600 °C, 700 °C, and 800 °C printed on the Photon printer and samples with a pyrolysis temperature of 700 °C printed on the Mono printer as a reference were measured in powdered form. The pyrolyzed sample in a pure state contains only the elements hydrogen, carbon, oxygen, and silicon.

The results of carbon and oxygen measurements and the calculation of hydrogen and silicon are summarized in Table 10 and illustrated in Figure 20. Overall, the values of carbon stay in a range of 1.3 %, and the deviation is low between all measurements. The oxygen values are in the range of 4.9 %, with a higher deviation compared to carbon.

Table 10: Results of the carbon & oxygen analysis and the calculation of the amounts of hydrogen and silicon.

	Photon @ 600 °C	Photon @ 700 °C	Photon @ 800 °C	Mono @ 700 °C
Carbon (wt.%)	28.1 ± 0.1	26.8 ± 0.1	26.7 ± 0.3	27.2 ± 0.2
Oxygen (wt.%)	30.0 ± 1.6	34.9 ± 1.6	34.1 ± 3.6	32.5 ± 1.6
Hydrogen + Silicon (wt.%)	41.9	38.3	39.2	40.3

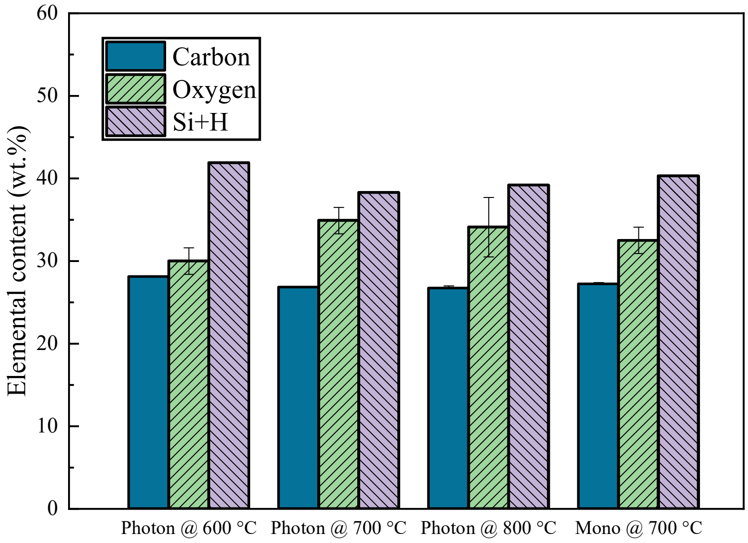

Figure 20: Results of the carbon & oxygen analysis and the calculation of the amounts of hydrogen and silicon.

Both measurement instruments from LECO are designed to analyze mostly steel samples. So, the measurement of elements that are not the main components of steel in high quantities is subjected to high errors. To determine the content of an element, first, a standard is measured, where a calibration curve is calculated. If the value of a measurement lies between zero and the maximum measured value of the calibration standards, the accuracy is high. But if the value lies beyond the curve, higher margins of error occur. In the case of carbon, the deviation of the measurements is low. It is common for steel samples to contain higher amounts of carbon, so if a standard with high concentrations is used, values of carbon, as seen in Table 10, in the range of 26 – 30 % can be accurately measured. This is not the case for the measurement system of oxygen. This element is an impurity for steels, which negatively affects their attributes even in amounts below one percent. So, the instrument for the oxygen measurements is designed for low amounts of oxygen. To compensate for this inaccuracy, the sample weighted was only a few milligrams, which is in the range of the scale error. This results in a high deviation of the oxygen measurements.

Overall, the results are as expected. As the polymer-to-ceramic conversion moves forward, primarily carbon and hydrogen, as organic compounds, leave the system and increase the amount of overall oxygen in the material.

5.4.2 Hydrophilicity

The amount of water and n-heptane adsorbed is measured via the mass to assess the hydrophilicity and hydrophobicity. Samples subjected to a pyrolysis temperature of 600 °C, 700 °C, and 800 °C printed on the Photon printer, and samples with a pyrolysis temperature of 700 °C printed on the Mono printer as a reference were measured as gyroids.

The results were summarized in Table 11 and illustrated in Figure 21. At higher pyrolysis temperatures, the adsorption of water increases while the adsorption of n-heptane decreases.

Table 11: Results of the hydrophilicity and hydrophobicity measurements.

	Photon @ 600 °C	Photon @ 700 °C	Photon @ 800 °C	Mono @ 700 °C
H_2O adsorbed (wt.%)	0.9	8.6	6.5	9.3
n-Heptane adsorbed (wt.%)	7.1	7.1	1.7	3
Ratio adsorbed (-)	0.1	1.2	3.8	3.1

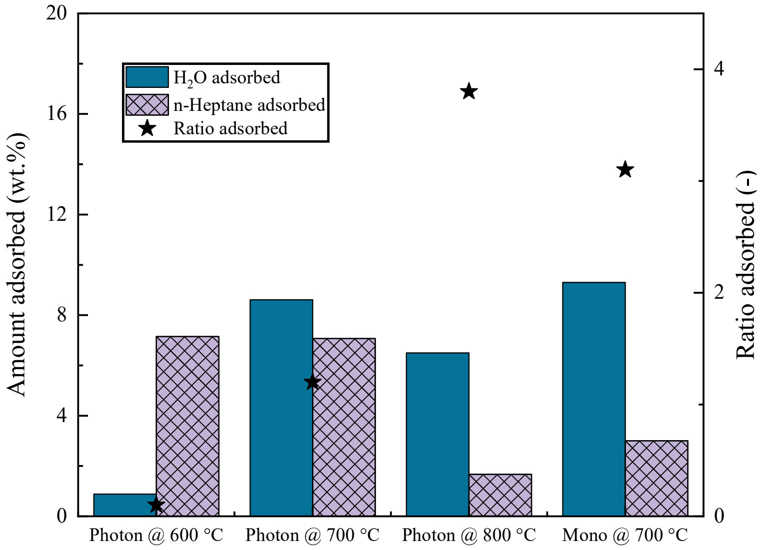

Figure 21: Hydrophilicity measured by adsorption of water and n-heptane of samples produced at different pyrolysis temperatures.

During the progress of the polymer-to-ceramic conversion, there is a certain point, at around 700 °C, as seen in Figure 21, where the characteristics of hydrophilicity and hydrophobicity reverse. It can be seen that the samples pyrolyzed at 600 °C show little affinity to water, by adsorbing as little as 0.9 wt.% with a ratio of 0.1 of water to n-heptane adsorbed. The amount of water adsorbed almost increases ten times when pyrolysis temperatures rise to 700 °C and the ratio increases to 1.2. When further increasing the pyrolysis temperature, the affinity for water decreases a little. However, the absorbance of n-heptane decreases almost fourfold and the ratio increases to 3.8. The samples produced with the Mono printer show similar values to those produced with the Photon printer pyrolyzed at 700 °C. The limitation is that the samples were not measured in powder form. This makes the measurement results more susceptible to the part geometry and printing parameters.

Overall, for the investigated PDC, an attribute switch of the surface is visible at the 700 °C pyrolysis mark. This knowledge can be used to tailor the attributes of hydrophilicity and hydrophobicity to the desired application.

5.4.3 Pore Size Distribution

The pore size distribution was measured to measure the range of micropores introduced via the phase separation. Samples were printed on the Photon printer with a pyrolysis temperature of 600 °C, 700 °C, and 800 °C. Samples with a pyrolysis temperature of 700 °C were printed on the Mono printer as a reference, and all samples were measured as cylinders. The raw data for the pore size distribution was directly taken from the measurement instrument. The data was taken directly from the measurement software Pascal and plotted to visually compare the different measurements in Figure 22. The pyrolysis temperature increases from the top to the bottom, and the samples pyrolyzed at the same temperature at 700 °C overlap. The following trends can be seen: the specific pore volume decreases with increasing pyrolysis temperature, while the relative pore volume and overall pore size distribution stays roughly the same.

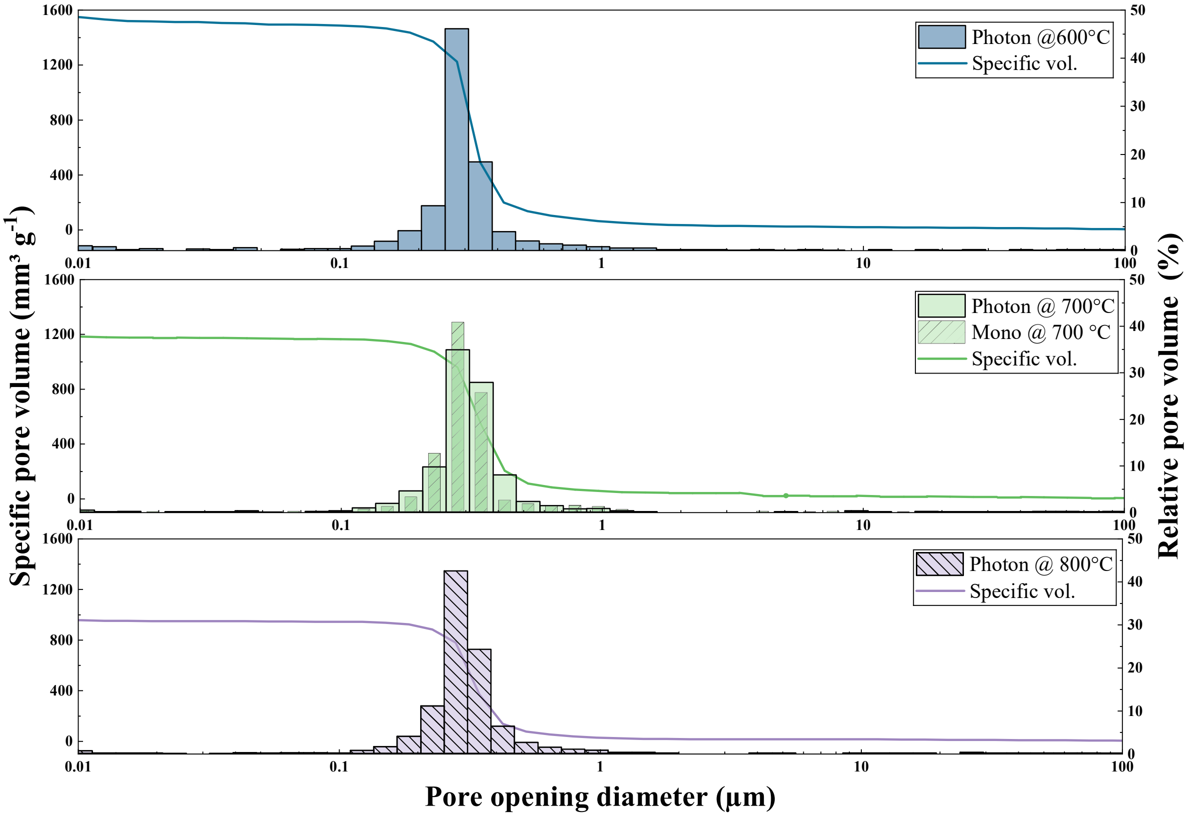

Figure 22: Specific and relative pore volumes for samples pyrolyzed at different temperatures and 3D printers.

The decrease of the specific pore volume at increasing pyrolysis temperatures is in line with what was expected when analyzing the linear shrinkage, which followed the same trend. When a porous material shrinks, the overall volume of the pores is sinking. If this shrinkage is of isotropic behavior, the pore size distribution shall not change, which is the observed behavior.

Overall, the distribution of the pore sizes is independent of the pyrolysis temperature, and only the specific pore volume is controllable through the pyrolysis temperature.

5.4.4 Permeability

Permeability measurements were conducted to predict and assess the laminar flow of gas and potentially liquids. Cylindrical samples, pyrolyzed at 600 °C, 700 °C, and 800 °C, printed on the Photon printer, and samples pyrolyzed at 700 °C printed on the Mono printer as a reference were measured and analyzed.

The results of these calculations are listed in Table 12 and illustrated in Figure 23.

The data shows that higher pyrolysis temperatures and higher values of k_1 and k_2 are attained for the samples produced with the Photon printer.

Table 12: Calculated permeability values for different pyrolysis temperatures and 3D printer used.

	Photon @ 600 °C	Photon @ 700 °C	Photon @ 800 °C	Mono @ 700 °C
k_1 (m^2)	$4.8\cdot10^{-15} \pm 9.7\cdot10^{-16}$	$4.7\cdot10^{-14} \pm 3.1\cdot10^{-14}$	$9.1\cdot10^{-14} \pm 5.5\cdot10^{-14}$	$6.1\cdot10^{-14} \pm 9.0\cdot10^{-15}$
k_2 (m)	$2.7\cdot10^{-12} \pm 1.1\cdot10^{-13}$	$5.2\cdot10^{-11} \pm 5.1\cdot10^{-11}$	$9.1\cdot10^{-11} \pm 8.3\cdot10^{-11}$	$6.1\cdot10^{-10} \pm 6.5\cdot10^{-12}$

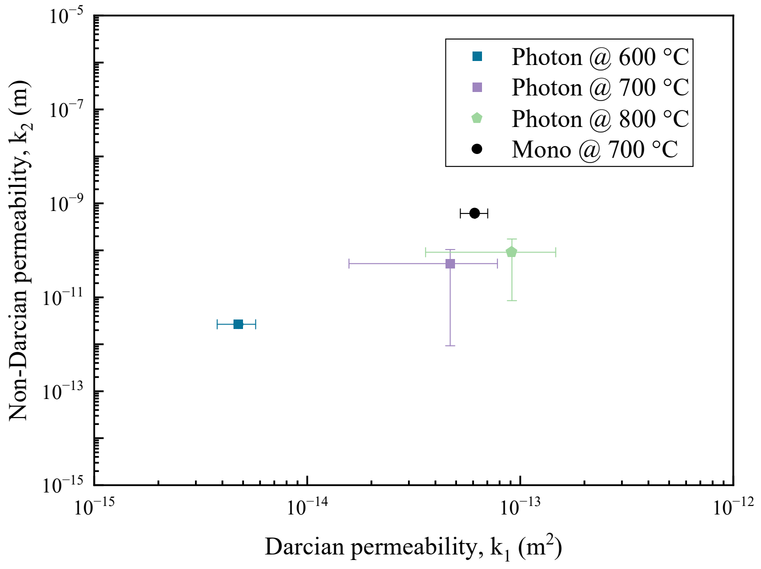

Figure 23: Calculated permeability values for different pyrolysis temperatures and 3D printer used in a double logarithmic representation.

The higher the values for k_1 and k_2, the better air can flow through the material. To evaluate the permeability, the k_1 was considered to be of higher importance and will be used further. The samples produced by the Photon printer at 800 °C and by the Mono printer at 700 °C show the highest values and let the most air permeate through them. However, this seems counterintuitive when comparing the data with the pore size distribution measurements in the previous chapter. The last chapter concluded that although all samples produced the same pore size distribution, the specific pore volume was higher in samples exposed to lower pyrolysis temperatures. This would lead to the assumption that the sample with the highest specific pore volume should be able to permeate the most air.

During the measurement of different samples, an observation was made. After measuring a sample, it was cut free from the shrink tube. Most of the samples produced with the Photon printer at 600 °C pyrolysis temperature would lose their structural integrity and crumble into small parts. Some of the structures broke away for samples that were exposed to a pyrolysis temperature of 700 °C, but the components mostly stayed intact. Samples produced at a pyrolysis temperature of 800 °C, could be cut free from the shrinking tubes without losing their shape. This observation leads to the following conclusion: Samples pyrolyzed at lower temperatures were compressed during the measurement and simulated lower permeability values than those samples, which could withhold the compressed air.

Overall, the samples produced with the Photon printer and made at 800 °C pyrolysis temperature showed the only reliable values. For the other samples, at least some material compression has taken place, which compromised the credibility of their values of k_1 and k_2.

5.5 PSO Substitution

5.5.1 General Processing

To widen the possibilities of manipulating and steering material characteristics, substitution experiments of the preceramic polymer were conducted. PSO1 was decreased in steps of 25 wt.% while adding PSO2 in equivalent amounts. The samples where substitution occurred are labeled according to the percentage of PSO2 used. All samples from this point on, if not stated otherwise, were produced with the Photon printer.

In this chapter, the same procedure of experiments and imaging as in Chapter 5.1, except the exposure intensity test, was conducted. Exposure tests were performed for the preceramic polymer and microscopic imaging for the green bodies after 3D printing. TGA, microscopic imaging, and FEG-SEM were conducted to oversee the pyrolysis process.

The exposure tests were conducted with the Photon printer. The results can be found in Table 13 and are depicted in Figure 24.

Table 13: Results of the exposure tests for the Photon printer. PSO1 substitution has taken place in 25 wt.% steps. The exposure time given is the time needed for a layer of 25 µm in thickness to be formed.

	Photon (s)
25 wt.% PSO2	8
50 wt.% PSO2	8
75 wt.% PSO2	9
100 wt.% PSO2	8

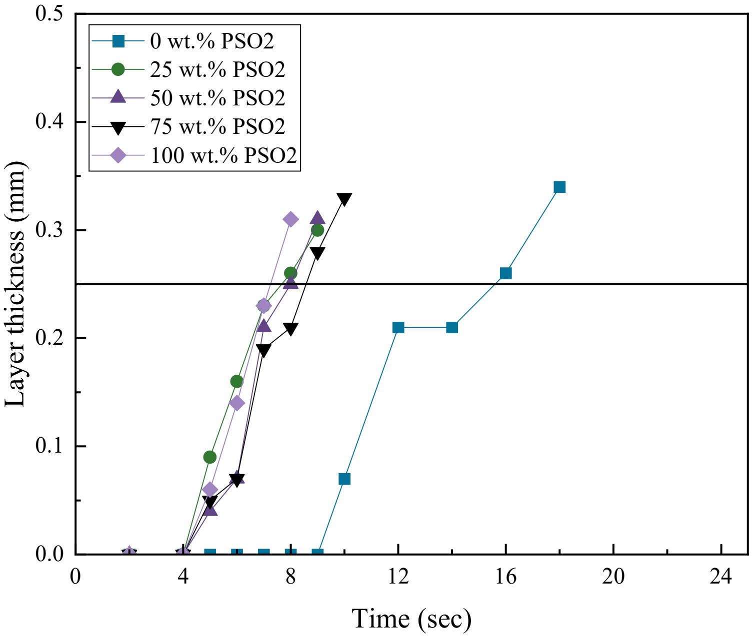

Figure 24: Time-dependent exposure tests to determine the time needed for a layer to reach 25 µm in thickness (marked with the horizontal line in the graph).

In comparison to the exposure time of resin of 15 seconds, which only contains PSO1, every level of substitution results in almost half of it for the photon printer. The difference between PSO1 and PSO2 lies in the difference of a rest group in the polymer. PSO1 contains a methyl rest and PSO2 and phenyl rest. Without further investigation, it is not possible to find a plausible answer to the cut of exposure time.

To protocol the process and the quality of the green bodies, **microscopic images** were taken. An example of a simple cylinder-shaped sample of 100 wt.% PSO2 can be seen in Figure 25.

Figure 25: 100 wt.-% PSO2 printed with the Photon printer (with an exposure time of 8 seconds per layer and a layer thickness of 25 µm per layer) and room temperature dried in the shape of a simple cylinder from the top covered with cracks.

Images for samples, with substitution of 25-,50-, and 75 wt.% resulted in similar quality and appearance as Figure 13. At 100 wt.% substitution, the samples appear transparent, as shown in Figure 25. This transparency is an indication of the absence of a phase separation. To validate this, FEG-SEM images of the pyrolyzed samples are needed.

To assess the suitability of the pyrolysis process for samples with substituted PSO1, **TGA** is conducted on resin of all substitution levels. The results are depicted in Figure 26.

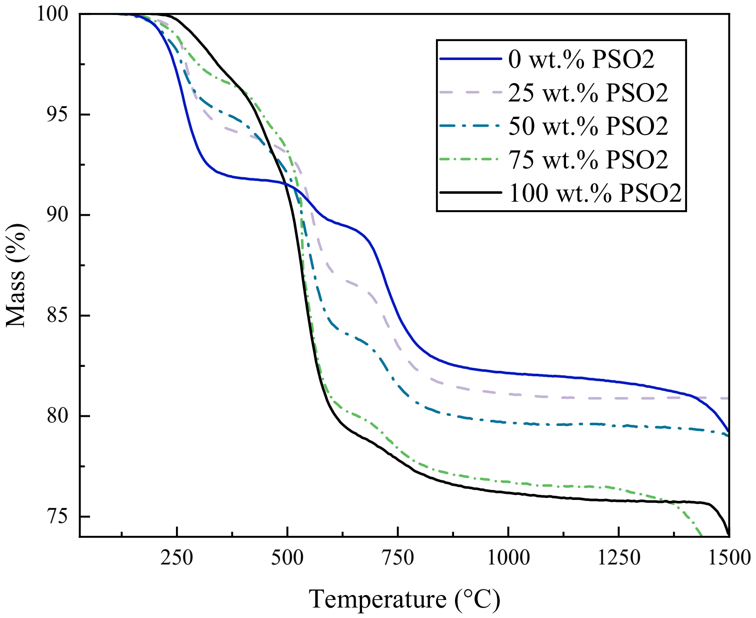

Figure 26: TGA measurement of PSO1 and all chosen substitution levels of PSO2 in powder form.

100 wt.% PSO2 is losing more than 5 percent more mass than PSO1 during pyrolysis. The reason for this lies behind the higher amount of organic compound. The phenyl group present in the PSO2 mostly turns into volatile organic components during the pyrolysis, leading to a higher mass loss overall. The rate of mass loss of PSO2 between 250 and 750 °C indicates an overlap of the crosslinking and the polymer-to-ceramic conversion. Also, it seems that crosslinking and the completion of the conversion process happen at higher temperatures than for PSO1. The substitution levels in between show a combined behavior of the pure composition. It was decided that the temperature profile for the substitution of PSO1 will not be adjusted, for its programming is already designed for removing organic components originating from the solvent and sacrificial monomer.

To protocol the process and the quality of the pyrolyzed ceramics, **microscopic images** were taken. An example of a simple cylinder of 100 wt.% PSO2 substitution and of a more complex honeycomb structure of 50 wt.% substitution can be seen in Figure 27.

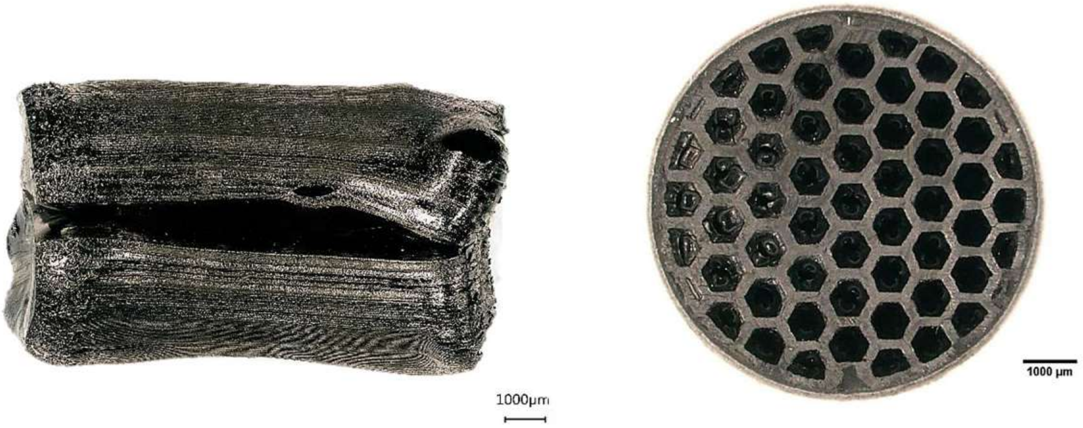

Figure 27: Images of a simple cylinder with 100 wt.-% PSO2 substitution pyrolyzed at 700 °C (left) and of a more complex honeycomb structure with 50 wt.-% substitution pyrolyzed at 800 °C (right). Both samples were printed on the Photon with an exposure time of 8 seconds per layer and a layer thickness of 25 µm per layer.

Samples were successfully pyrolyzed with a substitution of 100 wt.% of PSO2. Still, most of the samples were damaged with long cracks, as depicted in Figure 27 (left), or would break across when handling, indicating a missing connection between the individual printed layers. The long cracks and deformation indicate that the material's surface is densified. A non-porous surface would trap the emerging gases during the pyrolysis and create tension, leading to cracks and deformations. The shining and reflecting surface is another indicator for this to happen. This is also an indication of the absence of a phase separation. Samples with a substitution of 75 wt.% or lower showed no such behavior. An example is visible in Figure 27 (right). There, a 50 wt.% substituted resin was printed and pyrolyzed with high complexity. The sample surface was matte, and no deformations or cracks were visible. The gloss visible on the left side of the sample is most likely the residue of organic compounds, which could not evaporate out of the sample.

To validate the creation of hierarchical porosity, **FEG-SEM images** of the microstructure of 50 wt.% and 100 wt.% PSO2 substitution were taken. The surface and the cross-section of a sample fragment each, pyrolyzed at 700 °C, were captured at different resolutions. The images of the surfaces can be seen in Figure 28, and these of the cross-section in Figure 29.

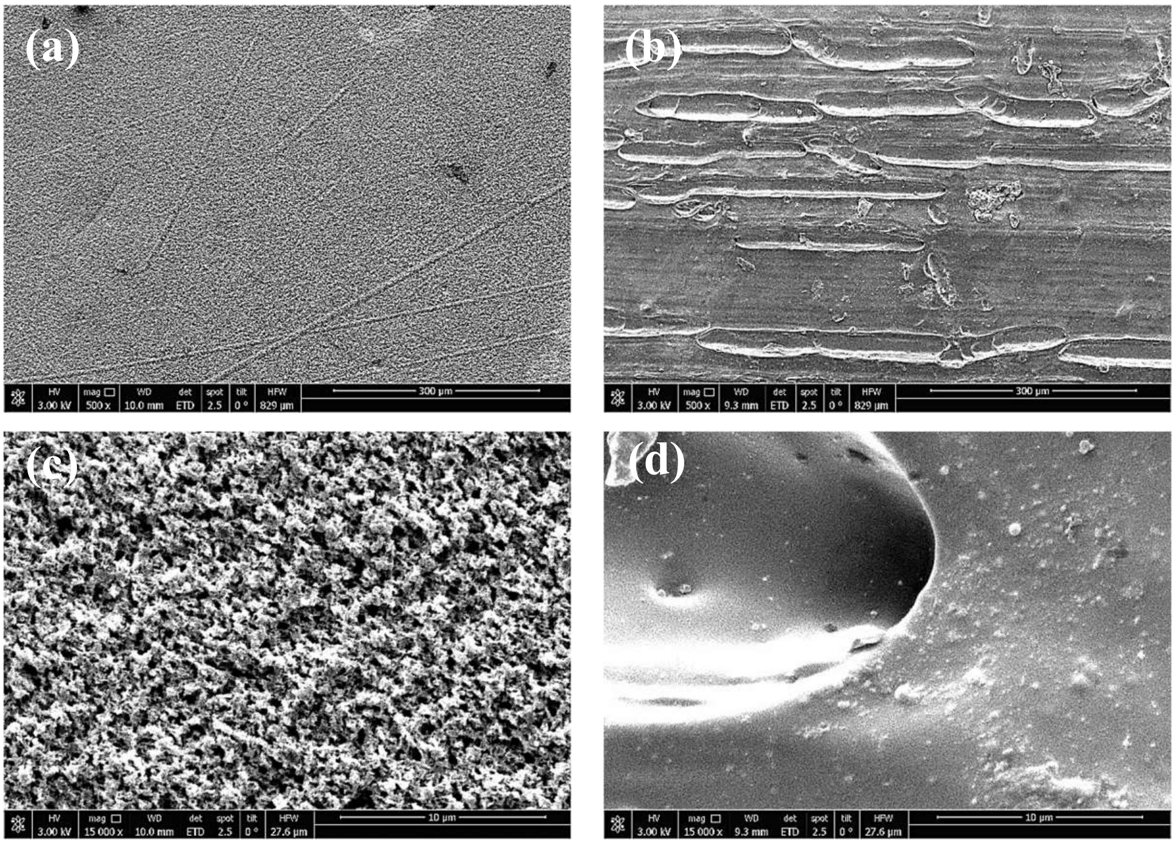

Figure 28: FEG-SEM images of the surface of a 50 wt.% PSO2 at lower (a) and higher (c) magnification pyrolyzed at 700 °C and of a 100 wt.% PSO2 substitution at lower (b) and higher (d) magnification pyrolyzed at 700 °C.

The prior observations indicated a successful phase separation for samples up to 75 wt.% PSO2 substitution. The images seen in Figure 28 (a & c) confirm these observations. A distributed pore structure can be seen. Compared with samples produced with PSO1, shown in Figure 16, a similar structure can be found, although the average pore size seems smaller. No porosity can be identified on the surface in the sample where 100 wt.% of PSO2 was substituted. A singular pore over 10 µm can be seen on the image with higher magnification. This is probably the result of emerging gases, which created this rupture while escaping out of the bulk. An analysis via mercury intrusion porosimetry shall give final confirmation of these observations.

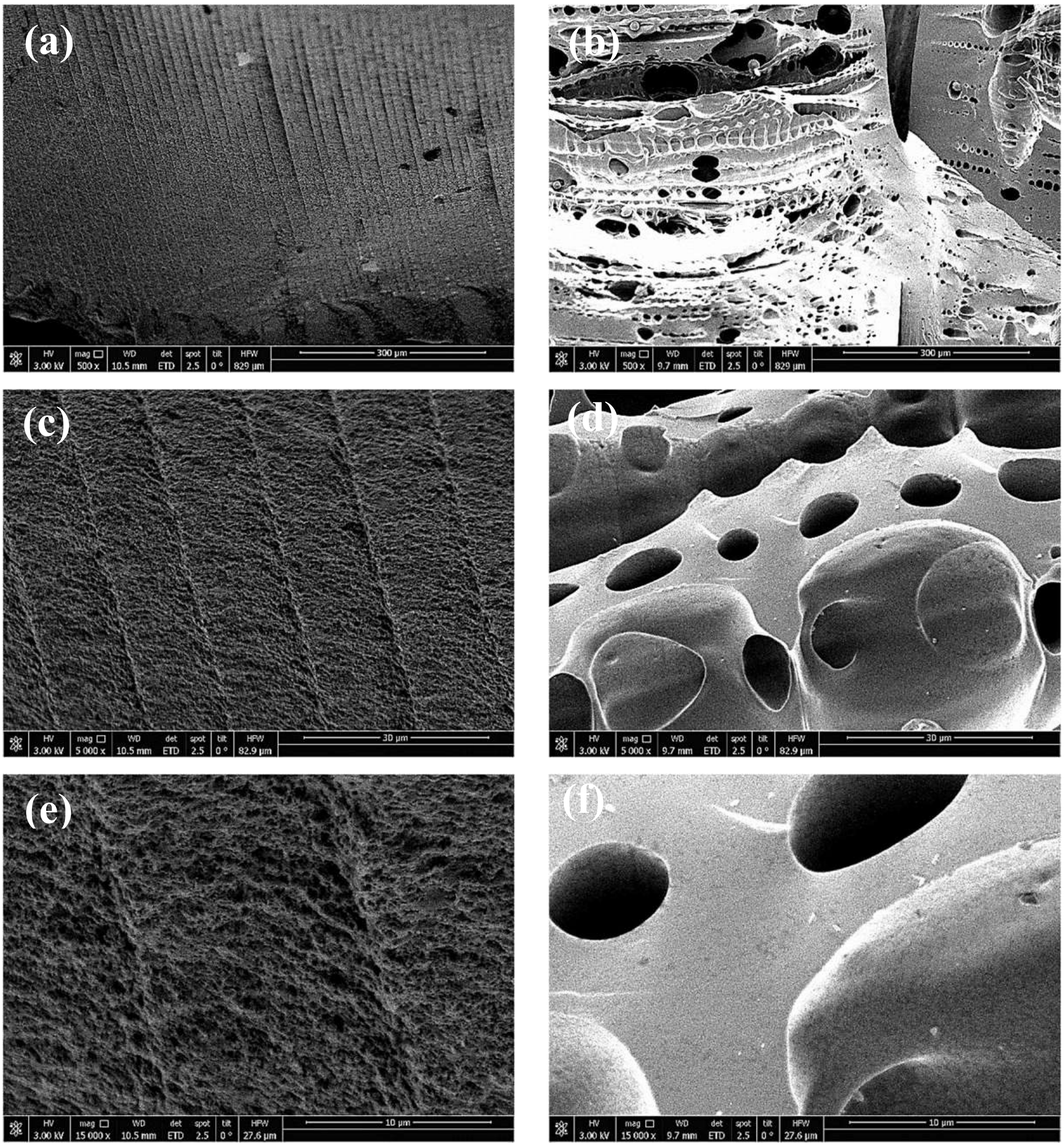

Figure 29: FEG-SEM images of the cross-section of a 50 wt.% PSO2 at lower (a), higher (c), and highest (e) magnification pyrolyzed at 700 °C and of a 100 wt.% PSO2 substitution at lower (a), higher (c), and highest (e) magnification pyrolyzed at 700 °C.

The images of samples with 50 wt.% PSO2 substitution seen in Figure 29 (a,c,e) shows finely distributed porosity, together with the remains of the layers, created by the 3D printing process. For the samples with 100 wt.% PSO2 substitution, different cracks, and deformations can be seen. The holes there fit with the observations made from the surface samples.

5.5.2 Ceramic Yield & Shrinkage

The ceramic yield and linear shrinkage were determined for samples with PSO substitution of 0, 25, 50, and 75 wt.% PSO2 at 600, 700, and 800 °C in double measurements. 100 wt.% PSO2 samples were not chosen due to their lack of shape stability. The calculations were conducted the same way described in Chapter 5.2 and given in Table 14. The ceramic yield and the linear shrinkage are plotted against the amount of substituted PSO2 in Figure 30 and Figure 31, respectively.

Table 14: Results of ceramic yield and linear shrinkage of samples with ascending wt.% of PSO2 substitution.

PSO2 subst. (wt.%) @ Pyrolysis temperature (°C)	Ceramic yield (%)	Lin. shrinkage xy (%)	Lin. shrinkage z (%)
0 @ 600	19.4	18.1	20.9
0 @ 700	19.6	24.6	29.3
0 @ 800	20.7	27.3	31.1
25 @ 600	20.4	25.7	29.5
25 @ 700	21.7	26.9	33.2
25 @ 800	20.1	27.8	35.2
50 @ 600	18.4	35.0	37.9
50 @ 700	20.3	38.2	42.0
50 @ 800	18.6	40.3	44.1
75 @ 600	18.3	42.3	34.3
75 @ 700	21.5	43.8	40.7
75 @ 800	20.0	45.9	42.9

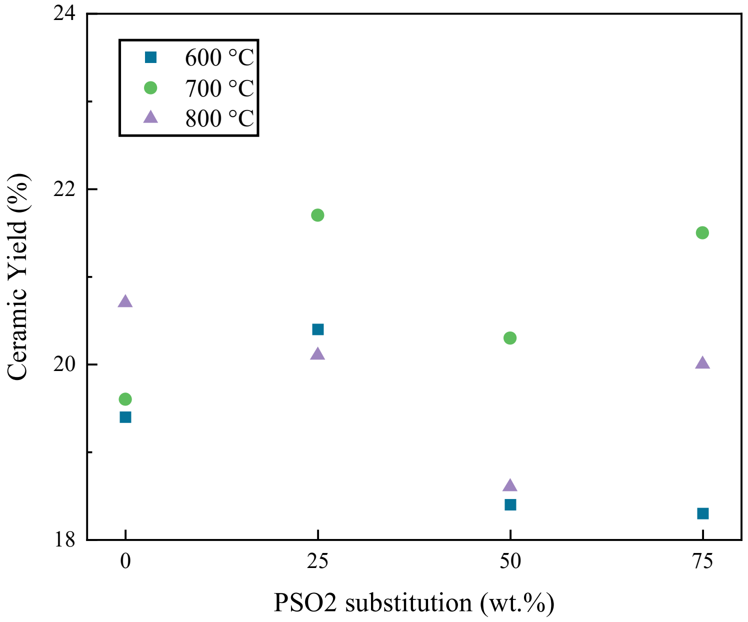

Figure 30: Ceramic yield of 0, 25, 50, and 75 wt.% PSO2 substitution.

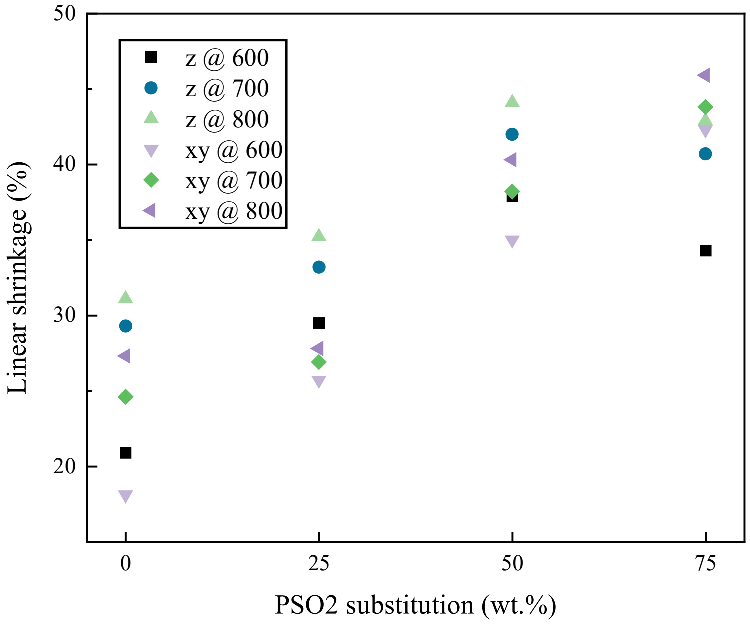

Figure 31: Linear shrinkage of 0, 25, 50, and 75 wt.% PSO2 substitution.

The **ceramic yield** does not correlate with the amount of substituted PSO2. However, as already discussed in Chapter 5.2, the amount of solvent used before pyrolysis and the time between 3D printing and pyrolysis seem to distort the results of the measurements. So, no clear statement about the correlation between ceramic yield and the amount of substituted PSO2 can be made.

The **linear shrinkage** increases with higher amounts of PSO2, as depicted in Figure 31. This would fit together with the data acquired with the TGA measurements. There, a higher quantity of PSO2 substitution results in an increase in mass loss during pyrolysis. This would also mean that the shrinkage of said material increases.

Overall, show the samples with substituted amounts of 25 and 50, and wt.% PSO2 handleability, successful phase separation, decreased printing times, and similar pyrolysis behavior as the samples, produced with no substitution. Samples with 75 wt.% PSO2 also shows similar behavior. However, the integral stability of the samples was lower. A few of the produced cylindric samples fell apart into smaller cylinders after pyrolysis. The higher linear shrinkage of samples with a higher amount of substituted PSO2 has to be considered, but it is not problematic during sample preparation.

5.5.3 Carbon Content & Hydrophilicity

The **carbon content** was measured for the 100 wt.% PSO2 substitution, pyrolyzed at 700 °C to determine the range in which the amount of carbon can vary. The measurements resulted in a value of 47.1 ± 0.9 % of elemental carbon. Therefore, depending on the amount of substituted PSO2, the amount of carbon can vary between 27 % and 47 % for samples pyrolyzed at 700 °C.

The **hydrophilicity and hydrophobicity** were measured for samples of 0, 25, 50, and 75 wt.% PSO2 substitution, with a pyrolysis temperature of 600 °C, 700 °C, and 800 °C as powders. The results are summarized in Table 15 and depicted in Figure 32.

Table 15: Results of the hydrophilicity measured by adsorption of water and n-heptane of samples with ascending wt.% of PSO2 substitution.

PSO2 subst. (wt.%) @ Pyrolysis temperature (°C)	H_2O adsorbed (%)	n-Heptane adsorbed (%)	Ratio adsorbed (-)
0 @ 600	0.9	7.1	0.1
0 @ 700	8.6	7.0	1.2
0 @ 800	5.4	1.7	3.9
25 @ 600	6.9	5.4	1.3
25 @ 700	13.2	7.2	1.8
25 @ 800	4.9	2.3	2.1
50 @ 600	3.1	13.3	0.2
50 @ 700	13.5	29.1	0.5
50 @ 800	10.2	3.8	2.6
75 @ 600	11.0	7.3	1.5
75 @ 700	22.8	4.2	5.4
75 @ 800	9.6	4.6	2.1

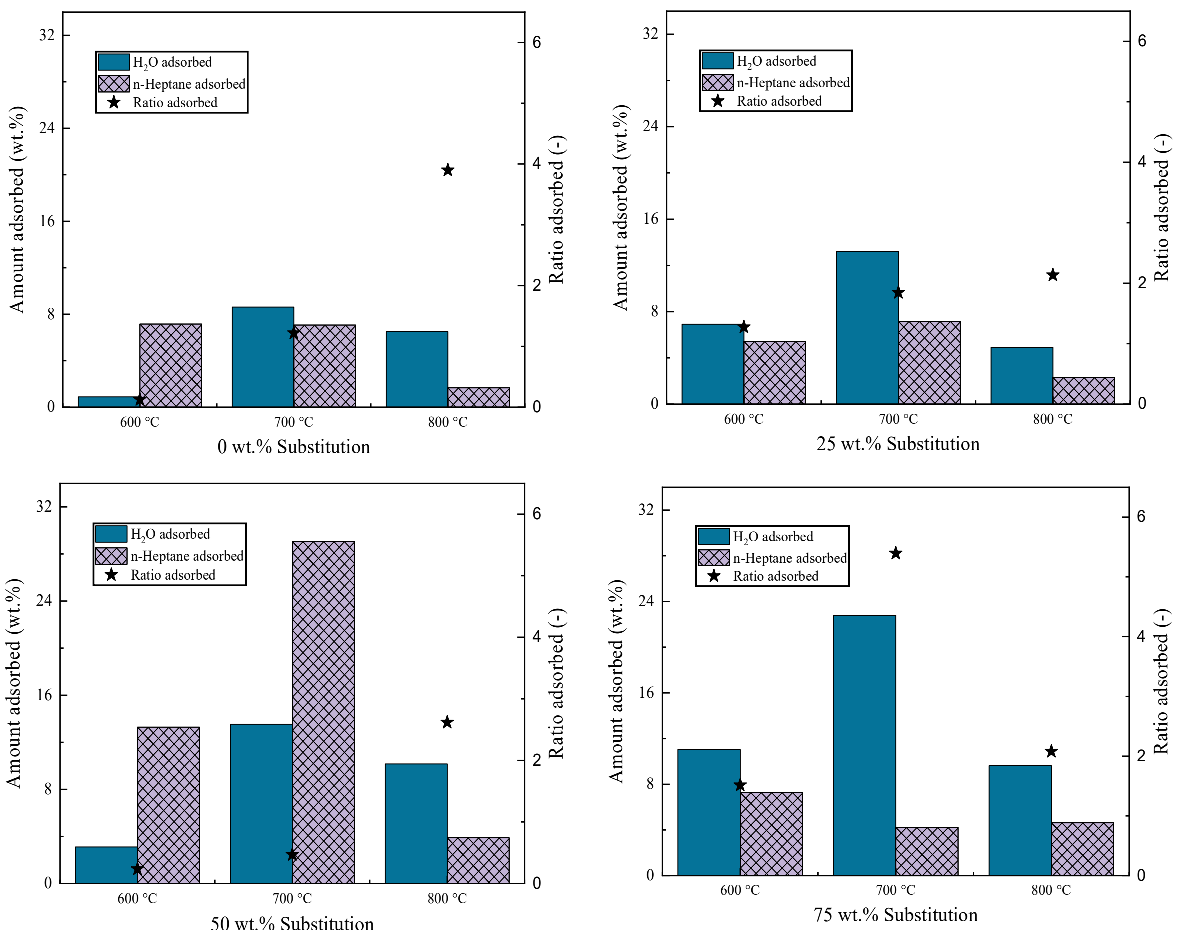

Figure 32: Hydrophilicity measured by adsorption of water and n-heptane of samples with different amounts of substituted PSO2. The y-axis scale was kept the same to enable a direct comparison.

Compared to Chapter 5.4.2, where the samples were measured as gyroids, the samples were milled into fine powder in this experiment. The expectation is an increase in overall adsorption caused by an increase in surface. This was not observed. The samples without substituting PSO2 resulted in almost the exact amounts of adsorbed water and n-heptane. The samples with a higher value of PSO2 substitution yielded an overall higher amount of adsorption. One reason for this change can be the increase in carbon with higher substitution levels. Another explanation could be a change in the pore size distribution, which will be analyzed in the next chapter. The n-heptane measurement of the 75 wt.% PSO2 sample has to be taken critically. There, after the reaction time was over, no n-heptane was left over in liquid form. This could mean that the desiccator ran out of vaporized n-heptane. So, the amount of adsorbed n-heptane is potentially higher than measured. No further statements can be taken until remeasuring the experiment.

5.5.4 Pore Size Distribution

The pore size distribution of samples, with 25, 50, 75, and 100 wt.% PSO2 substitution pyrolyzed at 700 °C was measured and plotted in Figure 33. The measurement for 100 wt.% PSO2 did result in no measured porosity and was not plotted.

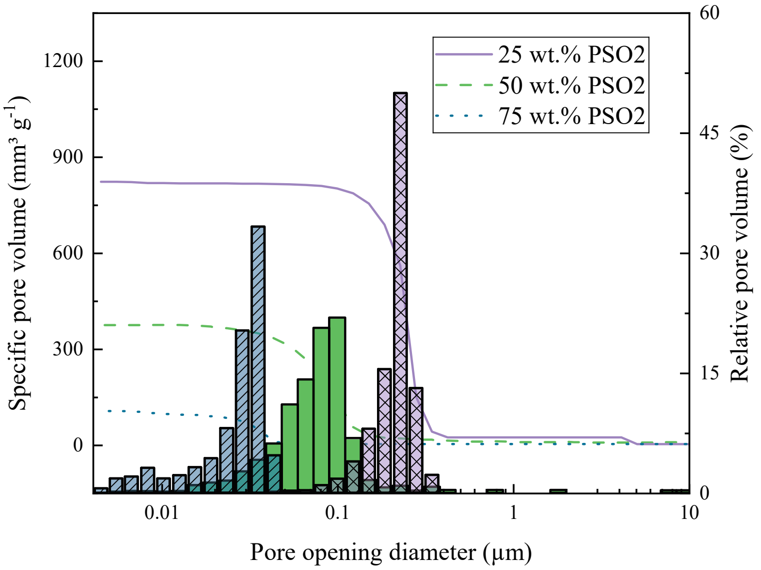

Figure 33: Specific and relative pore volumes for samples with 25, 50, and 75 wt.% PSO2 substitution pyrolyzed at 700 °C.

With an increasing substitution of PSO2, a decrease in specific and relative pore volume can be observed. This would confirm the observations made from the FEG-SEM images. No porosity was found on the surface or the cross-section. Also, for the images of a 50 wt.% PSO2 substituted sample, smaller and fewer pores could be seen compared to the unsubstituted sample. In Chapter 5.4.3, no change in pore size distribution was found when measuring samples of different pyrolysis temperatures. In this case, a change in the distribution is visible. Increasing substituted PSO2 shifts the pore size distribution to lower pore opening diameters to the nanoscale. This shift goes hand in hand with a decrease in specific pore volume, indicating a shrinkage of the pores and not a different mechanism. This behavior can also explain the increase of adsorption observed in the previous chapter, seen in Figure 32.

In this chapter, a way to control the pore size distribution was displayed. This enables many possibilities for manipulating the properties of the polymer-derived ceramic for specific applications and modifications.

5.6 Adsorption Experiments

This thesis used the adsorption of methylene blue (MB) as an application example for the materials prepared. First, the adsorption spectrum of MB, which was reported by Melgoza et al. ([34]; depicted in Figure 34) was investigated, and the peak of absorption was determined at 665 nm. This wavelength was used to determine the concentration of the dye, the calibration curve was measured in triplicates and is depicted in Figure 35. There, two linear regressions are fitted. The first regression is fitted into the linear area of the absorbance spectra with a measure of certainty of 0.998. Another linear regression is fitted into a part of the non-linear area of the spectra with a measure of certainty of 0.998. Measurement accuracy is given by the method until an absorbance of 1 is reached. The absorbance is depicted as a logarithmic scale. So, an absorbance of 1 means, that 90 % of light is absorbed by the measured substance, and for an absorbance of 2, 99 % of light is absorbed during the measurement.

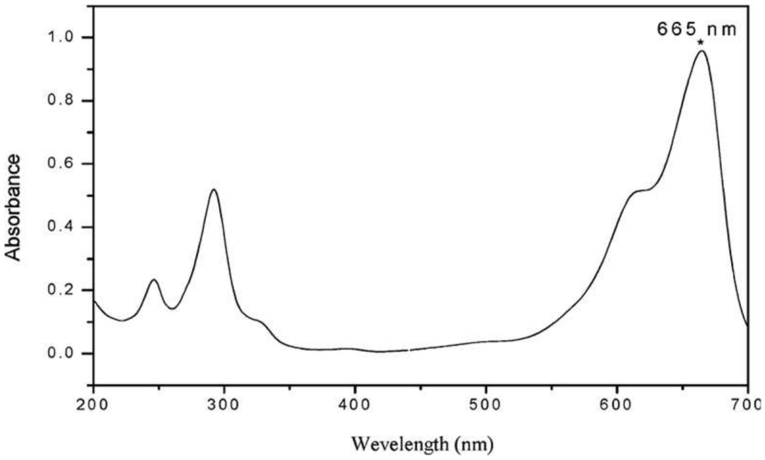

Figure 34: Absorbance spectra of methylene blue (50 mg·L^{-1}) [34]

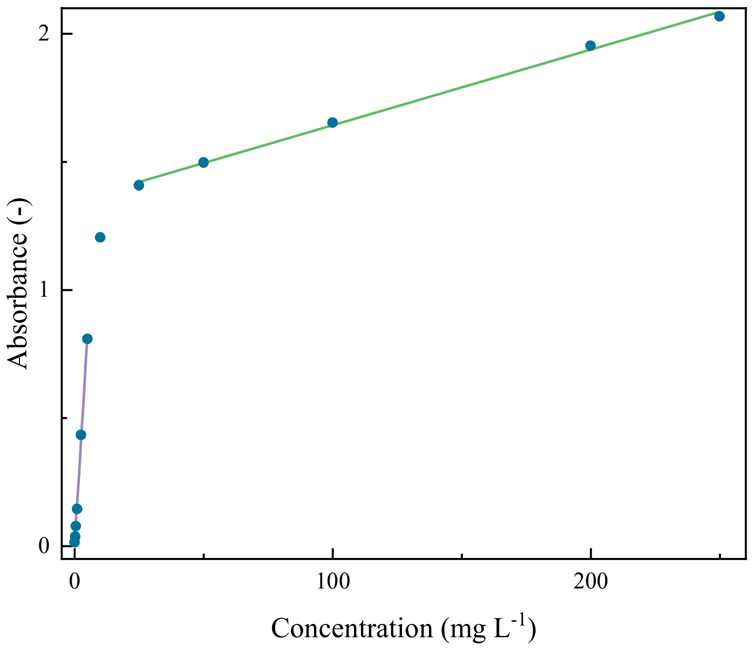

Figure 35: Absorbance measurement of a dilution series of methylene blue measured with UV/VIS spectroscopy at a wavelength of 665 nm. Two linear regressions were fitted into the linear area (purple) and the non-linear area (green).

The linear regression fitted at lower concentrations is used to determine low concentrations of methylene blue. The regression for the higher concentration is used to determine starting concentrations of > 10 mg·l^{-1}. The value is estimated via the regression because a linear fit was used for an area of non-linear behavior. The accuracy of both regression curves applies only to interpolated data.

Samples of different combinations of compositions of PSO, pyrolysis temperatures, shapes, and starting concentrations of dye were tested. Also, the influence of the flow rate was investigated. The starting and end concentrations were calculated with the rearranged functions resulting from the linear regression fitting in Table 16.

Table 16: Formulas for calculating an unknown concentration c with the absorbance (in short abs) as a free variable at a wavelength of 665 nm.

Linear area	Non-linear area
$c = 6.0753 \cdot abs + 0.0316$	$c = 333.33 \cdot abs - 449.03$

Each experiment is conducted separately, and the results influence the next sample choice. Samples formed as tubes are used as a baseline. The complex shape used is a cylindric gyroid, as seen in Figure 36. In industry, most organic molecules are filtered out by steps previous to adsorption. There, adsorbent materials are used to get rid of low concentrations of the dye. So, the requirements for these materials are high adsorbance values close to 100 %, while having high capacity allows more extended usage until resorption is necessary. The pH value of the diluted methylene blue solutions is measured to be around pH 6 and the temperature was at room temperature between 20 – 25 °C. The results of these calculations of every sample measured can be found in Table 17.

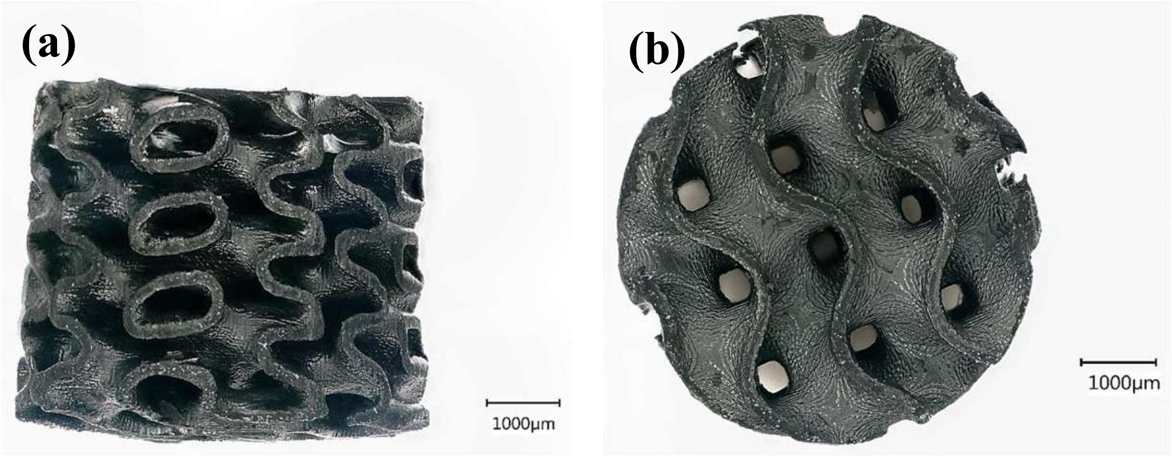

Figure 36: Cylindrical gyroid of a 25 wt.% PSO2 substituted pyrolyzed at 700 °C in front view (a) and top view (b).

Table 17: Results of the calculations of the dye adsorption experiments conducted with samples of varying composition, pyrolysis temperature, and shape at low and high flow rates after 24 hours exposure.

PSO2 subst. (wt.%) _ Pyrolysis temperature (°C) _ Shape	Initial concentration ($mg \cdot L^{-1}$)	q_t ($mg \cdot g^{-1}$)	R_{ads} (%)
	Flow rate of 0.5 $ml \cdot s^{-1}$		
0_700_Tube	1.2	0.19	47
0_700_Gyroid	1.2	0.18	45
0_700_Gyroid	5.0	0.26	9
0_800_Gyroid	1.0	0.37	84
25_800_Gyroid	1.1	0.39	70
	Flow rate of 3 $ml \cdot s^{-1}$		
0_700_Tube	0.9	0.02	6
0_600_Gyroid	2.4	0.07	9
0_800_Gyroid	2.2	1.30	71
25_700_Gyroid	2.2	1.00	63
25_800_Gyroid	13.2	3.85	52
50_800_Gyroid	4.7	1.84	91

Only a selected number of samples could be measured and analyzed due to time constrains. The flow rate has a high impact on capacity and adsorbance. Each measurement is given 24 hours of reaction time. A higher flow rate increases the interaction on the interface, increasing adsorbance. The increased flow rate also increases the pressure at which the dilution is pumped through the sample, increasing the interaction between adsorbent and adsorbate. The difference between the shape of a tube and a gyroid also strongly influences interface interaction. A higher surface area leads to higher interaction on the interface. The capacity was also influenced by the temperature at which the samples were produced. Those with a pyrolysis temperature of 800 °C outperform their counterparts pyrolyzed at 700 °C. The hydrophilicity measurements support these results. At 800 °C pyrolysis temperature, there is only a low amount of n-heptane adsorbed while maintaining high adsorbance values of water. So, samples with pyrolysis temperatures at 800 °C show high interactions with hydrophilic substances, which indicates the importance of the wettability of the adsorbent in an aqueous environment. The last variable also shows influence over the adsorption of methylene blue. Higher amounts of substituted PSO2 show a positive impact on the adsorption process. The change in pore size seen in Figure 33 could be the cause of this behavior, as well as the increase in carbon content.

An increase in flow rate, shape complexity, pyrolysis temperature, and change in composition all positively impact the capacity and adsorbance of the investigated material. However, although none of these factors were pushed close to their limits yet, this material shows potential in the field of wastewater purification. But in comparison to conventional adsorbent material, e.g., active carbon (e.g., 148.8 $mg \cdot g^{-1}$ in 5 minutes, [35]), there is still a noticeable gap in performance.

6 Summary & Outlook

Within the scope of this thesis, a previously developed phase separation resin formed by additive manufacturing and converted into a ceramic was investigated in terms of potential for wastewater purification applications. Throughout this investigation, the ability to steer and control specific attributes of the polymer-derived ceramic was highlighted. Also, new insights into the behavior of the resin during the shaping via additive manufacturing.

The production of phase-separated pyrolyzed SiOC ceramic bodies in simple and more complex bodies was successfully reproduced. Ceramic yield, linear shrinkage, pore size distribution, carbon-, and oxygen content were measured, resulting in values comparable to previous measurements of past colleagues.

During the reproducing process, an anomaly of linear shrinkage was found and investigated, which resulted in a conical shrinkage of the green bodies. Prior to this work, the reason for this anomaly was not found. The mainly used preceramic polymer, PSO1, has a higher affinity during the vat photopolymerization to be polymerized than the sacrificial agent TMPTMA. This leads to an impoverishment of PSO1 in the unformed resin. If not counteracted, this could lead to a difference in width of up to 20 % along the green body. Experiments following different approaches resulted in insights used to solve the problem of conical shrinkage. A dependency between the amount of the resin printed and the difference in the width of the green bodies was found. When using a maximum of 20 % resin for the shaping of the green bodies, conical shrinkage can be avoided.

The dependency of the maximum pyrolysis temperature and different characteristics of the material was investigated. Carbon – and oxygen content change according to the polymer-to-ceramic conversion with no significant shift in composition. The carbon amount decreased from 28.1 to 26.7 %, and the oxygen content increased from 30.0 to 34.1 % with increasing pyrolysis temperature. The hydrophilicity rises from 0.1 to 3.8 of ratio adsorbed, transitioning at 700 °C pyrolysis temperature, where both are at high values. The pore size distribution shows no significant difference, while the specific pore volume decreases from around 1600 to lower than 1000 $mm^3 \cdot g^{-1}$. The permeability measurements yielded k_1 values which increased from $4.75 \cdot 10^{-15}$ to $9.14 \cdot 10^{-14}$ m^2 with increased pyrolysis temperature. This is counterintuitive behavior due to the decreased pore volume measured, which can be explained by the lack of structural integrity of samples produced at lower pyrolysis temperatures.

Through the substitution of the already established PSO1 at different ratios of PSO2, the investigated characteristics could be varied even more. The carbon content can be increased by up to 47 %. This change influences the behavior of the hydrophilicity experiments. Samples with 75 wt.% PSO2 substitution can reach ratio adsorption values of 5.4. All substitution compositions that were investigated reached higher hydrophilicity values than those of the unsubstituted. The ability to control the pore size distribution was obtained. When increasing the amount of PSO2 in the composition, a shift to smaller pores was observed, even reaching the nanoscale.

The ability to control specific characteristics of the finished material and form complex structures was used to successfully perform dye adsorption experiments, reaching capacity values of up to 3.85 $mg \cdot g^{-1}$. These values are located at the low site compared to MB adsorption experiments conducted with active carbon, which e.g., reached values of 148.8 $mg \cdot g^{-1}$.

To sum up, insight into the shaping of green bodies increased the overall quality of the produced samples. With the combination of maximum pyrolysis temperatures and the difference in composition of the preceramic polymer, material characteristics like hydrophilicity and pore size distribution can be controlled. This material's ability to perform dyes' adsorption at continuous reactor conditions was proven and shown to be a future possibility of material choice in this field.

Investigating higher pyrolysis temperatures and substituting different PCP derivatives could provide even more flexibility in controlling the characteristics of the material and could be insightful.

The setup of the dye adsorption measurement can be improved to provide a better comparability to industrial applications. A different analytical instrument with a higher resolution could provide insight into adsorption kinetics. Also, different pH values, resorption, and reusability experiments should be conducted. Other dyes and heavy metals should also be tested and adsorption in a more complex matrix to provide a complete understanding of the material's possibilities in industrial applications.

References

1. Houghton, J., *Global warming.* Reports on Progress in Physics, 2005. **68**(6): p. 1343.
2. Gajdzik, B., et al., *The Influence of the Global Energy Crisis on Energy Efficiency: A Comprehensive Analysis.* Energies, 2024. **17**(4): p. 947.
3. Agrafiotis, C. and T. Tsoutsos, *Energy saving technologies in the European ceramic sector: a systematic review.* Applied Thermal Engineering, 2001. **21**(12): p. 1231-1249.
4. *Materialwissenschaft und Werkstofftechnik 12/2016.* Mat.-wiss. u. Werkstofftech, 2016. **47**(ISSN: 0933-5137): p. 1159.
5. Colombo, P., et al., *Polymer-Derived Ceramics: 40 Years of Research and Innovation in Advanced Ceramics.* Journal of the American Ceramic Society, 2010. **93**(7): p. 1805-1837.
6. Konegger, T., *Pores with a Purpose: Pore Tailoring Strategies in Polymer-Derived Ceramic Materials*. 2021, TU Wien.
7. *Verarbeitung von thermoplastischen Formmassen und Polyurethan-Rohstoffen*, in *Kunststoffe*. 2006. p. 267-325.
8. *Polymere in der additiven Fertigung*, in *Kunststoff-Wissen für die additive Fertigung*. p. 57-240.
9. Essmeister, J.G., *Photopolymerization-based processing of porous polymer-derived ceramics for catalysis applications*. 2023, Technische Universität Wien.
10. Bruzzoniti, M.C., et al., *Regenerable, innovative porous silicon-based polymer-derived ceramics for removal of methylene blue and rhodamine B from textile and environmental waters.* Environmental Science and Pollution Research, 2018. **25**(11): p. 10619-10629.
11. Bruzzoniti, M.C., et al., *Polymer-derived ceramic aerogels as sorbent materials for the removal of organic dyes from aqueous solutions.* Journal of the American Ceramic Society, 2018. **101**(2): p. 821-830.
12. Zeydanli, D., S. Akman, and C. Vakifahmetoglu, *Polymer-derived ceramic adsorbent for pollutant removal from water.* Journal of the American Ceramic Society, 2018. **101**(6): p. 2258-2265.
13. Zhao, C., et al., *Defects Engineering with Multiple Dimensions in Thermoelectric Materials.* Research, 2020. **2020**: p. 9652749.
14. McCusker, L., F. Liebau, and G. Engelhardt, *Nomenclature of structural and compositional characteristics of ordered microporous and mesoporous materials with inorganic hosts (IUPAC Recommendations 2001).* Pure and Applied Chemistry, 2001. **73**(2): p. 381-394.

15. Eisenberg, D., et al., *The evolution of hierarchical porosity in self-templated nitrogen-doped carbons and its effect on oxygen reduction electrocatalysis.* RSC Advances, 2016. **6**(84): p. 80398-80407.

16. Schwieger, W., et al., *Hierarchy concepts: classification and preparation strategies for zeolite containing materials with hierarchical porosity.* Chemical Society Reviews, 2016. **45**(12): p. 3353-3376.

17. Caro, J., *Hierarchy in inorganic membranes.* Chemical Society Reviews, 2016. **45**(12): p. 3468-3478.

18. Zhu, Y., et al., *Hierarchical porous ceramic membrane with energetic ozonation capability for enhancing water treatment.* Journal of Membrane Science, 2013. **431**: p. 197-204.

19. Essmeister, J., et al., *Stereolithography-based additive manufacturing of polymer-derived SiOC/SiC ceramic composites.* Journal of the European Ceramic Society, 2022. **42**(13): p. 5343-5354.

20. Salmang H., S.H., *Keramik*. 7., vollständig neubearbeitete und erweiterte Auflage ed. 2007: Berlin, Heidelberg : Springer-Verlag Berlin Heidelberg.

21. Essmeister, J., et al., *Hierarchically Porous Ceramic and Metal-Ceramic Hybrid Materials Structured by Vat Photopolymerization-Induced Phase Separation.* Advanced Materials Technologies, 2024. **9**(1): p. 2301400.

22. Crittenden, J.C., et al., *MWH's water treatment: principles and design*. 2012: John Wiley & Sons.

23. Mihelcic, J.R. and J.B. Zimmerman, *Environmental engineering: Fundamentals, sustainability, design*. 2021: John Wiley & Sons.

24. Hojamberdiev, M., et al., *Polymer-derived mesoporous SiOC/ZnO nanocomposite for the purification of water contaminated with organic dyes.* Microporous and Mesoporous Materials, 2012. **151**: p. 330-338.

25. Hojamberdiev, M., et al., *Template-free synthesis of polymer-derived mesoporous SiOC/TiO2 and SiOC/N-doped TiO2 ceramic composites for application in the removal of organic dyes from contaminated water.* Applied Catalysis B: Environmental, 2012. **115-116**: p. 303-313.

26. Pan, J., et al., *Porous SiOC composites fabricated from preceramic polymers and wood powders for efficient dye adsorption and removal.* Research on Chemical Intermediates, 2017. **43**(7): p. 3813-3832.

27. Yu, Z., et al., *Polymer-derived mesoporous Ni/SiOC(H) ceramic nanocomposites for efficient removal of acid fuchsin.* Ceramics International, 2017. **43**(5): p. 4520-4526.

28. Pan, J., et al., *Difunctional hierarchical porous SiOC composites from silicone resin and rice husk for efficient adsorption and as a catalyst support.* Colloids and Surfaces A: Physicochemical and Engineering Aspects, 2020. **584**: p. 124041.

29. Fuchsberger, A.-M., *Polymer-derived ceramics with hierarchical porosity by phase serperation*. 2023, TU Wien.

30. Abell, A.B., K.L. Willis, and D.A. Lange, *Mercury Intrusion Porosimetry and Image Analysis of Cement-Based Materials.* Journal of Colloid and Interface Science, 1999. **211**(1): p. 39-44.

31. Scheffler, M. and P. Colombo, *Cellular ceramics: structure, manufacturing, properties and applications*. 2006: John Wiley & Sons.

32. Kocjan, A., T. Konegger, and A. Dakskobler, *Hierarchical macroporous–mesoporous γ-alumina monolithic green bodies with high strength.* Journal of Materials Science, 2017. **52**(19): p. 11168-11178.

33. Szoldatits, E., et al., *Polymer-derived SiOC as support material for Ni-based catalysts: CO2 methanation performance and effect of support modification with La2O3.* Frontiers in Chemistry, 2023. **11**: p. 63503.

34. Melgoza, D., A. Hernandez-Ramírez, and J. Peralta-Hernández, *Comparative efficiencies of the decolourisation of Methylene Blue using Fenton's and photo-Fenton's reactions.* Photochemical & Photobiological Sciences : Official Journal of the European Photochemistry Association and the European Society for Photobiology, 2009. **8**: p. 596-9.

35. El-Bery, H.M., et al., *High adsorption capacity of phenol and methylene blue using activated carbon derived from lignocellulosic agriculture wastes.* Scientific Reports, 2022. **12**(1): p. 5499.

Appendix

Table A1: Measurement data of the exposure intensity measurements for every measurement point, depicted in Figure 8, and 3D printer. The exposure intensity was measured with an Ocean Optics spectrometer.

	Power Density / mW·cm^{-2}					
Measurement Points	Photon D2	Mars 2P	Mono 4K @ 25 %	Mono 4K @ 50 %	Mono 4K @ 75 %	Mono 4K @ 100 %
1	1.35	1.46	0.93	1.18	1.47	1.83
2	1.41	1.53	0.82	1.42	1.33	1.62
3	1.31	1.53	0.78	1.13	1.49	1.51
4	1.36	1.56	1.12	1.48	1.9	2.39
5	1.34	1.52	1.03	1.28	1.64	2.13
6	1.32	1.34	0.99	1.9	1.54	1.88
7	1.3	1.34	0.96	1.26	1.63	1.99
8	1.31	1.32	0.97	1.24	1.67	2.05
9	1.29	1.28	0.95	1.3	1.62	1.94
Average ± Deviation	1.33 ± 0.04	1.44 ± 0.10	0.95 ± 0.10	1.35 ± 0.23	1.59 ± 0.16	1.94 ± 0.27